Keratin isoform shifts modulate motility signals during wound healing

Benjamin A Nanes [1,2,✉], **Kushal Bhatt**[2], **Evgenia Azarova** [2,3], **Divya Rajendran** [2], **Tadamoto Isogai** [2], **Kevin M Dean** [2], **and Gaudenz Danuser** [2,✉]

[1]Department of Dermatology, UT Southwestern Medical Center, Dallas, TX, USA
[2]Lyda Hill Department of Bioinformatics, UT Southwestern Medical Center, Dallas, TX, USA
[3]Present address: Department of Materials Science and Engineering, Johns Hopkins University, Baltimore, MD, USA
✉ Correspondence to *benjamin.nanes@utsouthwestern.edu* or *gaudenz.danuser@utsouthwestern.edu*

Abstract

Keratin intermediate filaments form strong mechanical scaffolds that confer structural stability to epithelial tissues, but the reason this function requires a protein family with fifty-four isoforms is not understood. During skin wound healing, a shift in keratin isoform expression alters the composition of keratin filaments. How this change modulates cellular function to support epidermal remodeling remains unclear. We report an unexpected effect of keratin isoform variation on kinase signal transduction. Increased expression of wound-associated keratin 6A, but not of steady-state keratin 5, potentiated keratinocyte migration and wound closure without compromising epidermal stability by activating myosin motors. This pathway depended on isoform-specific interaction between intrinsically disordered keratin head domains and non-filamentous vimentin shuttling myosin-activating kinases. These results substantially expand the functional repertoire of intermediate filaments from their canonical role as mechanical scaffolds to include roles as signaling scaffolds that spatiotemporally organize signal transduction cascades depending on isoform composition.

Introduction

Effective tissue barrier formation depends on keratin intermediate filaments[1]. Joined through desmosomes, keratin filaments form strong trans-cellular networks, which function as mechanical scaffolds[2]. Fifty-four different keratin isoforms are expressed in an intricate pattern depending on issue, anatomic site, and differentiation state[3]. Keratin filaments are particularly important in the skin, where their disruption causes epidermal fragility in a number of diseases[4]. However, epidermal stability must be balanced with plasticity[1]. Too much stability relative to plasticity can limit remodeling, resulting, for example, in non-healing wounds[5]. Too much plasticity relative to stability can result in uncontrolled or abnormal remodeling, a feature of numerous skin diseases ranging from cancer to psoriasis[6,7]. The molecular mechanisms underlying the balance between epidermal stability and plasticity largely remain to be uncovered.

During wound healing, the required balance between epidermal stability and plasticity shifts, as keratinocytes change shape, migrate into the wound area, and reform the epidermal architecture[1]. These tissue-level processes are accompanied at the cellular scale by increased expression of five *wound-associated keratin* isoforms: keratin 6A (K6A), K6B, K6C, K16, and K17 [8-10]. Expression of wound-associated keratins also increases in other situations with elevated epidermal remodeling, including psoriasis[11,12], squamous cell carcinoma[13], hypertrophic scars[14], and following tissue expander placement[15].

While the selective expression of wound-associated keratins implies specialized functions in epidermal remodeling, identifying the roles individual keratin isoforms play in specific cellular processes has been experimentally and conceptually challenging. Depleting or mutating individual keratins frequently disrupts keratin filament architecture and the more general mechanical scaffold function[16]. Partial redundancy between keratin isoforms further complicates the interpretation of monogenic models[17]. Wound-associated keratin knock-out mice often demonstrate prominent defects in epidermal integrity and keratinocyte cell-cell adhesion, but lack generalized wound-healing defects[18-21]. Similarly, disease-causing mutations in human wound-associated keratin genes broadly disrupt epidermal stability where the affected isoform is expressed[22,23]. Thus, while wound-associated keratins contribute to the canonical intermediate filament mechanical scaffold, it is less clear if additional functions of these isoforms specifically promote plasticity during epidermal remodeling.

In order to disentangle the specific contributions of wound-associated keratins to epidermal remodeling from the general function of keratin mechanical scaffolds, we took a gain-of-function rather than a loss-of-function approach. We found that increased expression of wound-associated K6A, but not steady-state K5, potentiated keratinocyte migration without compromising cell-cell adhesion. Rather than altering the mechanical response to external force, K6A expression increased cellular force generation via activation of actomyosin contractility. This role in signal transduction was mediated by preferential interaction of the K6A intrinsically disordered head domain with non-filamentous vimentin. K6A-enriched keratin filaments and non-filamentous vimentin transiently anchored a signaling complex, spatially organizing regulatory kinases and myosin subunits to promote myosin activation. Thus, by wound-induced keratin isoform switching, epidermal cells amplify

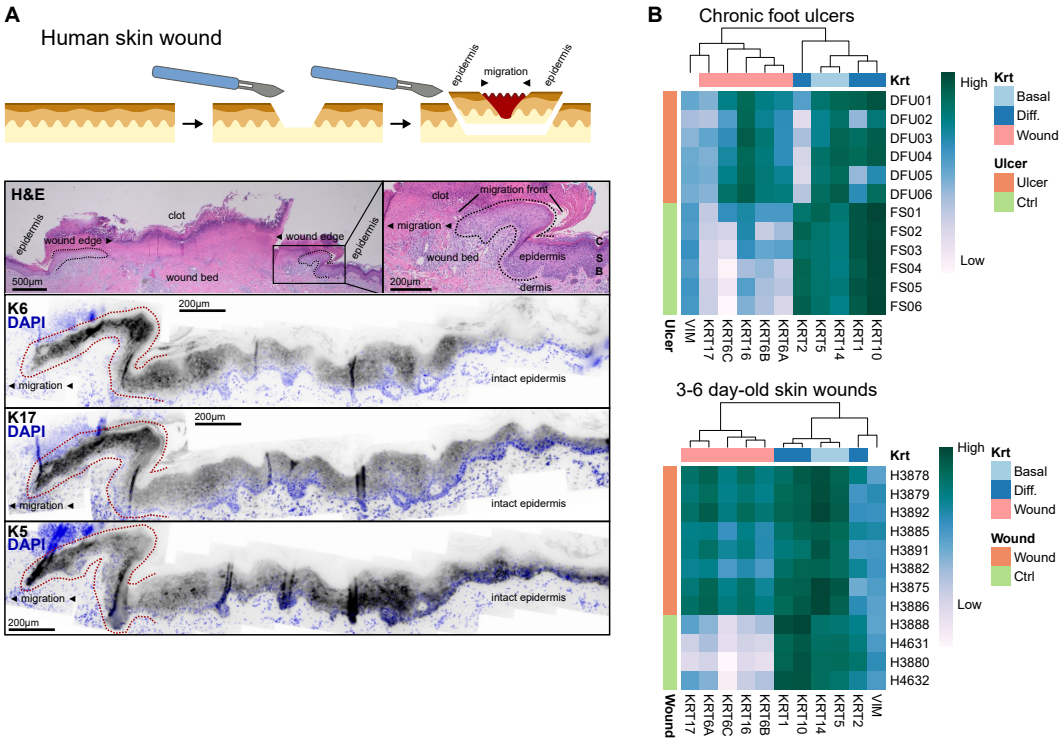

Figure 1. Epidermal remodeling triggers a keratin isoform switch.

A. Top: Schematic diagram of a skin excision following a diagnostic biopsy, which includes healing edges from the biopsy wound. Middle: Hematoxylin and eosin (H&E)-staining. Dotted outlines, epidermal migration fronts. Epidermal layers: B, basal; S, spinous (suprabasal); C, cornified. Bottom: Immunofluorescence labeling of wound-associated K6 and K17, and steady-state basal epidermal K5. Left, healing wound edge; Red dotted outline, epidermal migration front; Right, intact epidermis.

B. Intermediate filament expression in human skin wounds. Top: Microarray analysis of chronic diabetic foot ulcers and intact skin controls (GSE80178). Right: Bulk RNA sequencing of experimentally created punch biopsy wounds and intact skin controls (GSE97615).

and spatially organize a signal transduction cascade that promotes critical functions for the wound healing process. These results highlight the complex interplay between the cytoskeleton and apparently diffuse pools of cytoplasmic proteins to spatiotemporally structure biochemical reactions.

Results

Wound-induced keratin switching in an epidermal culture model

Keratin expression change following wounding has been observed in animal models and humans[8-10]. We reproduced these findings in a human skin excision specimen, where we detected increased expression of wound-associated K6 and K17 at healing wound edges (Figure 1A). We also reanalyzed published transcriptomics data of acute[24] and chronic wounds[25] with a focus on intermediate filament expression and found strongly increased expression of all five wound-associated keratin genes (Figure 1B). However, wound-induced keratin switching has not previously been observed in cultured keratinocytes. Furthermore, cultured keratinocytes often express wound-associated keratins at baseline[26], possibly reflecting the increased proliferative rate of keratinocytes in culture[27]. This has complicated efforts to understand the implications of keratin switching at the cellular and subcellular levels.

Consistent with prior reports[28,29], we found that an hTERT and Cdk-4 immortalized human keratinocyte cell line grown in submerged monolayer culture expressed steady-state basal level keratins K5 and K14 and wound-associated K6 and K17 (Figure S1A). Steady-state differentiated keratins K1 and K10 were barely detectable (Figure S1A), as expected for a basal keratinocyte phenotype. Immunofluorescence of monolayer scratch wounds did not show any change in expression of K6 or K17 relative to K5 at the wound edge (Figure 2A-B). Similarly, bulk qRT-PCR did not show any change in wound-associated keratin transcript levels in scratched keratinocyte monolayers compared to unwounded controls (Figure 2C).

While keratin expression remained stable in submerged monolayer culture, keratinocytes at an air-liquid interface formed a multilevel structure undergoing differentiation, with increased expression of K10 in the upper layers (Figure 2D-E), closely resembling the stratified squamous architecture of the epidermis[30]. We leveraged these stratified epidermal cultures to create a three-dimensional wound model. Cultures were grown within a barrier mold, followed by barrier removal to allow keratinocyte migration (Figure 2F). In stark contrast to monolayer scratch wounds, wound-associated K6 and K17 expression was notably increased at the migrating edge of stratified cultures (Figure 2F). The presence of wound-induced keratin switching in the epidermal culture model prompted us to more closely examine the function of wound-associated keratins in this system.

Wound-associated K6A supports epidermal migration

We sought an interventional strategy for modulating relative levels of wound-associated versus steady-state ker-

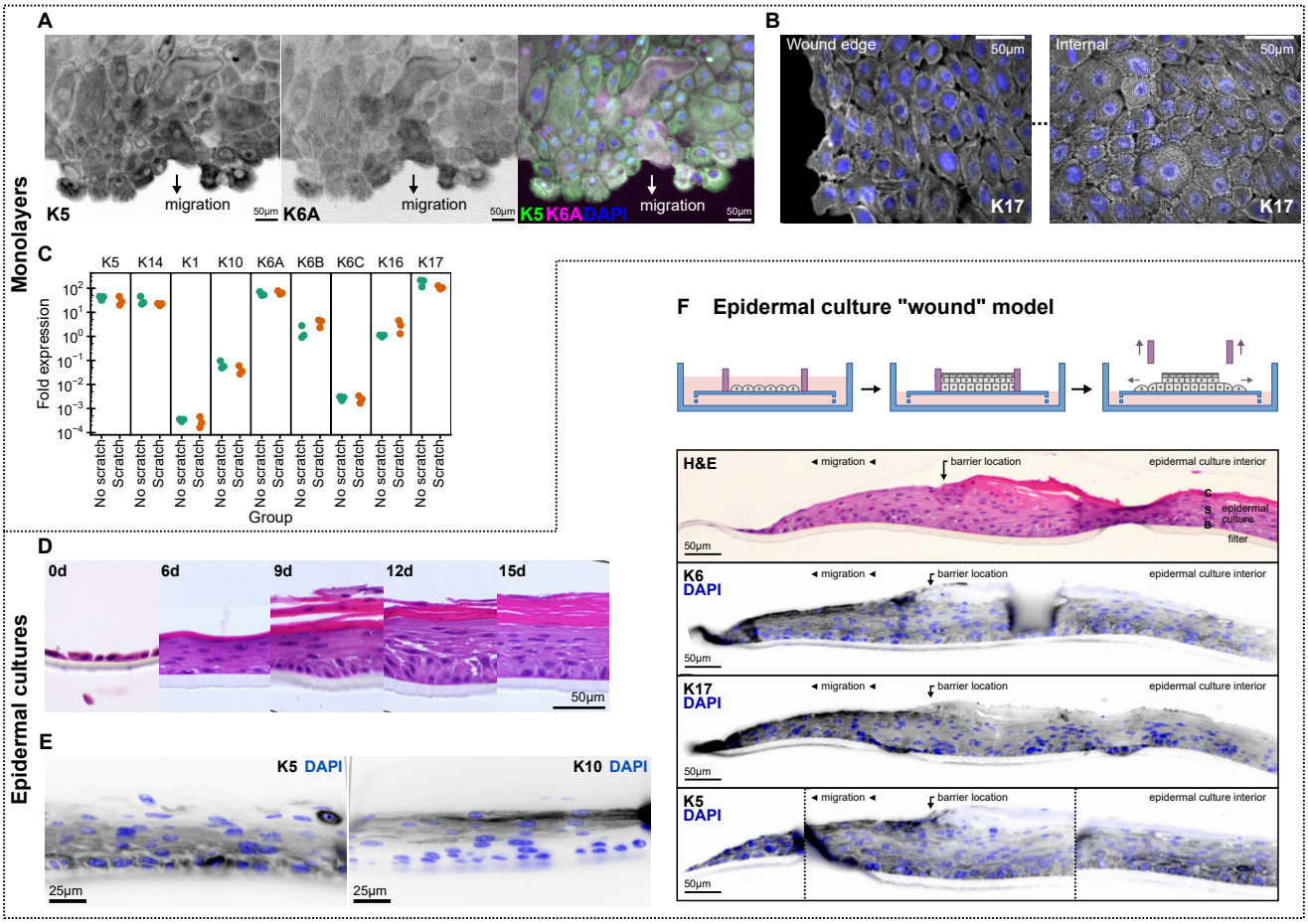

Figure 2. Remodeling triggers keratin isoform switching in three-dimensional epidermal cultures.

A-B. Confluent keratinocyte monolayers were scratched with a pipette tip to create wounds, allowed to migrate for 24-hours, then fixed, labeled for immunofluorescence of steady-state K5 and wound-associated K6 (C) or K17 (D), and imaged. In (D), images of the migration edge and monolayer interior were acquired with the same illumination and detection settings.

C. Keratinocyte monolayers were preserved intact or repeatedly scratched with a pipette tip (see Methods), then processed for RNA isolation and quantification of keratin transcript levels by qRT-PCR. Individual keratin transcript levels were compared to the average level of all keratin transcripts measured. n = 3 monolayers per group.

D-E. Keratinocytes were cultures at an air-liquid interface to induce stratification. D, Hematoxylin and eosin (H&E) staining after different growth periods. E, Immunofluorescence labeling of a basal epidermal keratin, K5, and a differentiated epidermal keratin, K10.

F. Top: Schematic diagram of the epidermal culture wound model. Removal of a barrier mold allows keratinocytes from the stratified culture to migrate into the "wound" area (see Methods). Middle: H&E staining after 72 hours of migration. Arrow, prior location of the barrier. Epidermal layers: B, basal; S, spinous (suprabasal); C, cornified. Bottom: Immunofluorescence labeling of wound-associated K6 and K17, and a steady-state basal K5. Left, migration edge; Right, epidermal culture interior. Dashed vertical lines, image re-alignment correcting for folds in the tissue section.

atins. Prior attempts to knock down or delete keratin genes have resulted in prominent loss of cell-cell adhesion and decreased mechanical integrity[31-34]. To circumvent such global effects, we took a gain-of-function approach and co-expressed fluorescently tagged K6A, a wound-associated keratin, and K5, the closest steady-state paralog to K6A, and used fluorescence activated cell sorting to isolate cell populations with different relative keratin expression (Figure 3A).

We created K5^{high}/K6A^{low} (K5^{high}) and K5^{low}/K6A^{high} (K6A^{high}) cell lines with moderately increased (approximately 35%) levels of each keratin (Figures 3B and S1B). Increasing K5 or K6A protein levels did not change endogenous protein or transcript levels of other keratins (Figure S1C-D) or affect cell proliferation (Figure 3C). Importantly, K5^{high} and K6A^{high} cells maintained equivalent cell-cell adhesion capacity, with similar junction morphology and thickness on transmission electron microscopy (Figure 3D), similar numbers of desmosomes and adherens junctions (Figure 3E), and similar monolayer strengths as measured by dispase fragmentation assays (Figure 3F).

We then proceeded to test the migration potential of K5^{high} and K6A^{high} keratinocytes. In three-dimensional epidermal migration assays, K6A^{high} epidermal cultures migrated farther than K5^{high} epidermal cultures over a 12-hour period (Figure 3G). We further took advantage of the bright fluorescence signals from the tagged keratins to enable live imaging of paired K5^{high} and K6A^{high} epidermal cultures following removal of a separating barrier (Figure 3H). While the partially translucent polycarbonate filter limited image quality, the fluorescence signal was sufficient to identify and track the migration edges using custom software (Figure 3H and Video 1)[35]. We observed that K6A^{high} epidermal cultures moved faster into the gap than their K5^{high} counterparts, and K6A^{high} cultures maintained their migration advantage over a 20-hour migration period (Figure 3I-

K). Therefore, increased expression of wound-associated K6A offers a significant benefit to wound closure in three-dimensional epidermal cultures.

Wound-associated K6A supports migration in monolayers and individual cells

In order to perform high-resolution imaging of potential differences in cytoskeletal organization and dynamics between K5^{high} and K6A^{high} cells, we turned to a monolayer wound healing assay. However, in contrast to the three-dimensional epidermal wound model, we were initially unable to identify a clear difference in migration speed between K5^{high} and K6A^{high} monolayers (Figure S2A-D and Video 2). Since the monolayer migration assay had significant wound-to-wound variability (Figure S2B), we wondered whether subtle but systematic differences in migration behavior between individual K6A^{high} and K5^{high} cells were missed in the coarser population level analysis.

To test this possibility, we created a mosaic population of keratinocytes including K5^{high}, K6A^{high}, K5^{high}/K6A^{high}, and K5^{low}/K6A^{low} cells and performed live imaging of the

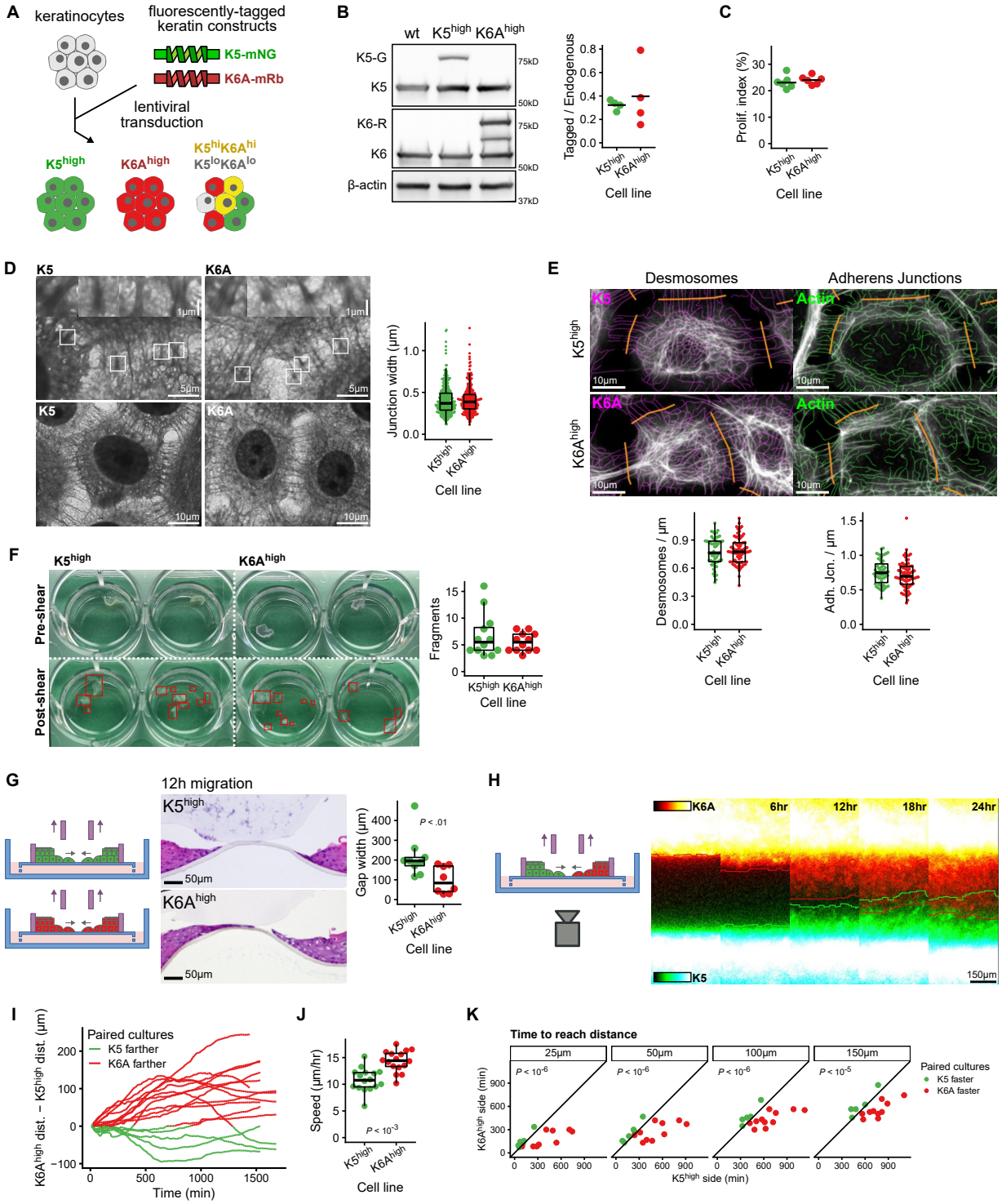

monolayer wound healing response (Figure 4A and Video 3). We applied particle image velocimetry to track local migration throughout the monolayer (Figure 4B, bottom; Video 3, right)[35] and segmented the monolayers into different keratin expression regions (Figure 4B, top; Video 3, left), permitting comparison of migration speeds between keratin expression regions within the same wound and controlling for between-wound variability.

All wounds followed a similar pattern. After scratching the monolayer with a pipette tip, the overall migration speed rapidly increased to a peak followed by slow deceleration, though the height and timing of the peak varied between experimental repeats (Figure 4C). Around the time of the overall migration speed peak, K6A^{high} regions exhibited a small, but consistent, migration advantage (Figure 4D). In the large majority (31 of 36) of wounds, K6A^{high} regions had higher speeds than K5^{high} regions (Figure 4E). K6A^{high} regions also had higher speeds than K5^{high}/K6A^{high} and K5^{low}/K6A^{low} regions, and K5^{high}/K6A^{high} regions had higher speeds than K5^{high} regions, indicating a dose-dependent effect (Figure 4E). Interestingly, the K6A^{high} migration advantage was transient. By 2 hours after the migration peak, K5^{high} region speeds began to approach those of the K6A^{high} regions (Figure 4F and Video 4). Consistent with these results, K6A^{high} cells were modestly enriched near the wound edge of a mosaic population monolayer fixed after 18-hours of migration (Figure S2E).

Given that K5^{high} and K6A^{high} keratinocytes retain similar cell-cell adhesion properties (Figure 3D-F), we asked whether the K6A^{high} migration advantage was solely an emergent property of collective migration or if it could also be detected in individual keratinocytes. To address this question, we seeded K5^{high} and K6A^{high} cells at low density and tracked their movement over 12-hours using live imaging (Figure 4G and Video 5). Much like in the monolayer migration assays, K6A^{high} cells displayed a small advantage in migration speed and displacement, which peaked 4 to 8-hours after seeding (Figure 4G-I). Also similar to monolayer migration, the migration advantage was temporary, with the differences between K5^{high} and K6A^{high} cells becoming less apparent by 8 to 12-hours after seeding (Figure 4G-I). Thus, wound-associated K6A transiently potentiates keratinocyte migration at least in part through a cell autonomous effect.

Wound-associated K6A alters keratin filament dynamics

To address how the relative levels of keratin isoforms affect migration, we examined possible differences in keratin filament organization between K5^{high} and K6A^{high} cells. We imaged keratin filaments over time and used a computer vision pipeline to segment the filament networks (Figure 5A-B and Video 6)[36]. In snapshots, the K5^{high} and K6A^{high} filament networks were similar. K5^{high} filament networks appeared to contain a somewhat higher number of very short filaments (Figure S3A), and an associated slight increase in overall filament density (Figure S3B), compared to K6A^{high} networks, possibly reflecting a slight difference in the imaging properties of the two fluorescent tags. Filament curvature was indistinguishable between K5^{high} and K6A^{high} cells (Figure S3C-E). However, when analyzed over time, K5^{high} filaments displayed larger intracellular displacements than K6A^{high} filaments (Figure 5A-B).

To quantify differences in filament network dynamics, we created a metric reflecting changes in position and orientation of filaments between timepoints at one-minute intervals[36]. Each point on the filament network at baseline is scored by the distance and difference in orientation of the nearest filament in the next considered timepoint (Figure 5C). We then smoothed the local scores to generate continuous filament dynamics score maps and averaged over individual cells (Figure 5D). Comparing K5^{high} to K6A^{high} cells, we found that K6A systematically decreased intracellular dynamics of keratin filaments (Figure 5E). We confirmed that the difference in filament dynamics between K5^{high} and K6A^{high} cells could not be explained by the small differences in number of very short filaments or filament density (Figure S3F-G).

We further extended this approach using two-color live imaging of K5^{high}, K6A^{high}, and K5^{high}/K6A^{high} cells, allowing us to segment and calculate filament dynamics scores

Previous page: **Figure 3. Wound-associated K6A supports epidermal migration without compromising mechanical stability.**

A. Schematic diagram of the gain-of-function keratin expression model. Cultured keratinocytes were transduced with lentivirus to express tagged K5 and K6A, then divided by fluorescence activated cell sorting into different populations including those with high levels of K5 (K5^{high}), high levels of K6A (K6A^{high}), high levels of both keratins (K5^{hi}K6A^{hi}), and low levels of both keratins (K5^{lo}K6A^{lo}).

B. Western blot analysis of endogenous (K5, K6) and exogenously expressed (K5-G, K6-R) keratins in parental (wt), K5^{high}, and K6A^{high} cell lines (see also Figure S1B). Right: Ratio of K5-G or K6-R to K5 or K6. *n* = 4 samples per group.

C. Proliferation of K5^{high} and K6A^{high} cells in culture measured by uptake of 5-ethynyl-2'-deoxyuridine (EdU) during a 60-minute incubation. Proliferation index, defined as the percentage of nuclei with EdU incorporation. *n* = 6 samples per group.

D. Transmission electron micrographs of K5^{high} and K6A^{high} monolayers. Insets highlight typical electron-dense cell-cell junction complexes. Right, distribution of junction complex widths. *n* = 314-348 junctions from 40-41 images per group.

E. Fluorescence imaging of K5^{high} and K6A^{high} cell monolayers with segmentation of keratin and actin filament networks. Desmosomes and adherens junctions were identified, respectively, by keratin and actin filament bridges between adjacent cells. *n* = 55-71 cell-cell borders from 17-18 images per group.

F. Mechanical stability of keratinocyte monolayers measured using a dispase-based fragmentation assay (see Methods). *n* = 12 monolayers per group.

G. Paired epidermal cultures separated by a 500-µm barrier were grown from K5^{high} and K6A^{high} cells. Following removal of the barrier and 12-hours of migration, the remaining gap width was measured in H&E-stained tissue sections. *n* = 8-9 epidermal culture pairs per group.

H-K. Live imaging of epidermal migration. Paired epidermal cultures separated by a 500-µm barrier were grown with K5^{high} and K6A^{high} cell lines on opposite sides of each barrier. Following barrier removal, cells were imaged over 24 hours (H; see also Video 1; see Methods). Red and green lines, farthest migration extent of the K6A^{high} and K5^{high} culture halves at each time point. I, Difference in migration distance, defined as farthest distance migrated by the K6A^{high} half minus farthest distance migrated by the K5^{high} half. Each line represents one culture pair. J, Average migration speed over 20-hours, defined as farthest migration distance divided by total time. K, Time needed to reach the designated distance checkpoint. Dots represent culture pairs, with x- and y-axis location corresponding to time required for the K5^{high} and K6A^{high} halves to reach the designated distance. Dots blow the diagonal represent culture pairs where the K6A^{high} half reached the designated distance checkpoint first; dots above the diagonal represent culture pairs where the K5^{high} half reached the checkpoint first. *n* = 16 epidermal culture pairs.

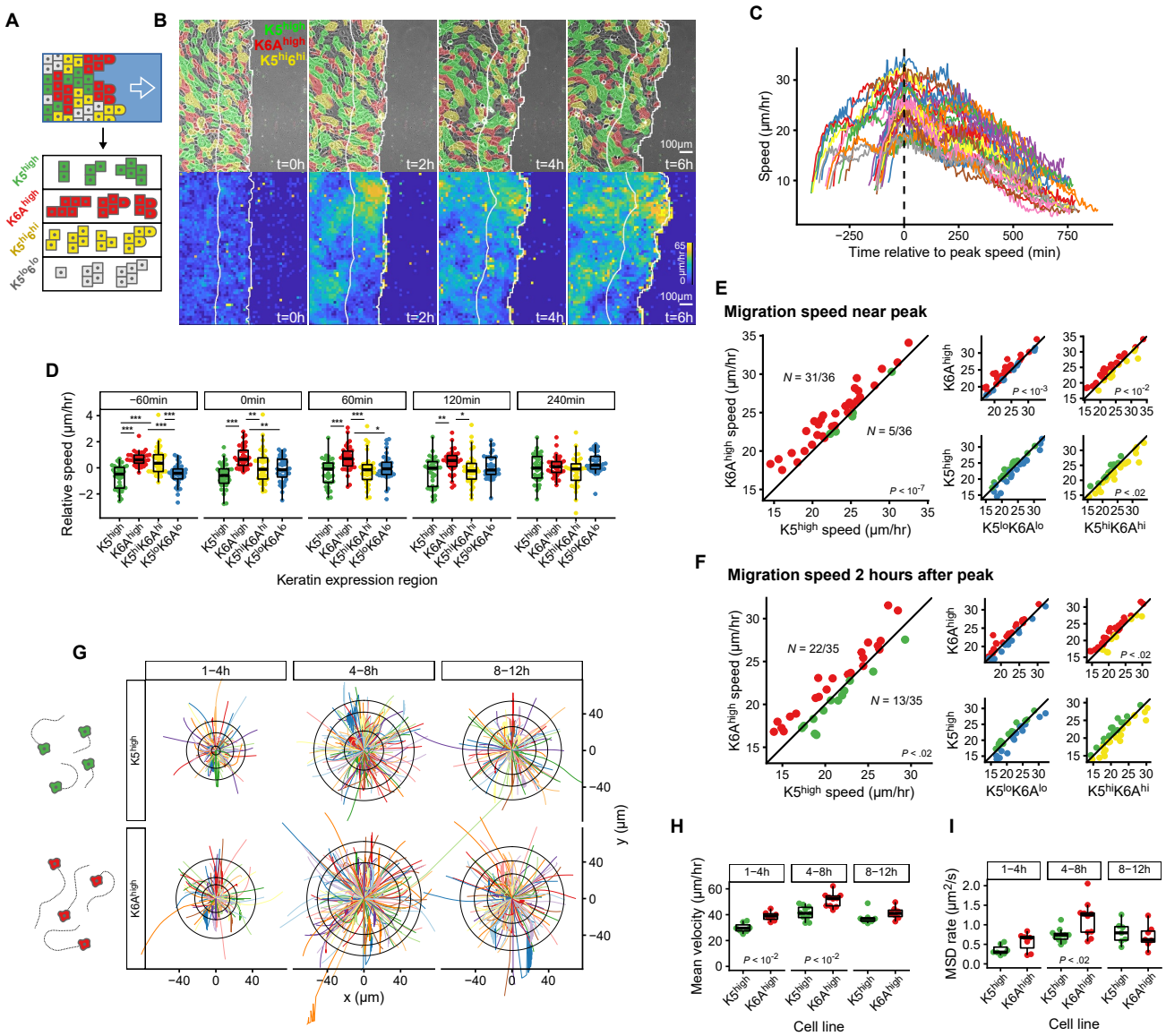

Figure 4. Wound-associated K6A supports keratinocyte migration in monolayers and single cells.

A. Schematic diagram of a mosaic monolayer containing K5^{high} (green), K6A^{high} (red), K5^{high}/K6A^{high} (K5^{hi}6^{hi}, yellow), and K5^{low}/K6A^{low} (K5^{lo}6^{lo}, grey) cells during migration. Local migration speeds are compared between different keratin expression regions.

B. Top: Keratin expression regions. Bottom: Local migration speeds calculated using a computer vision pipeline (see Methods). White lines, 200-μm band tracking the wound edge. See also Video 3.

C. Time courses of average local migration speed 10-μm to 200-μm from the wound edge aligned relative to the global peak in migration speed. n = 36 scratch wounds.

D. Relative local migration speed within each keratin expression region at different time points relative to the peak in migration speed. Relative local speeds are defined as the local migration speed for a keratin expression region minus the average migration speed across all regions 10-μm to 200-μm from the migration edge. n = 36 scratch wounds.

E-F. Pairwise comparison of average local migration speed between keratin expression regions at the peak in migration speed (E) and 2-hours later (F). Each point represents one scratch wound, with x- and y-axis location corresponding to the migration speed in different keratin expression regions. n = 36 scratch wounds. See also Video 4.

G-I. Movement of sparsely seeded, individual K5^{high} and K6A^{high} keratinocytes. G, Cell trajectories aligned at the initial position, including the first hour of each track within the time window. Rings, quantiles of maximum distance from the origin. See also Video 5. H-I, Mean track velocity (H) and mean squared displacement rate (I) in K5^{high} and K6A^{high} cells. n = 7-10 movies with 144-232 tracks per group.

for K5 and K6A simultaneously (Figure S3H-M and Video 6). We found a dose-dependent effect of K6A on filament dynamics, with the highest dynamics scores for K5^{high} cells, the lowest dynamics for K6A^{high} cells, and intermediate dynamics for K5^{high}/K6A^{high} cells (Figure S3L). Furthermore, we could compare filament segmentations and dynamics scores between the K5 and K6A channels in K5^{high}/K6A^{high} cells. Given the known propensity for individual keratins to intermix within filament networks[37], K5 and K6A network segmentations overlapped considerably, as expected (Figure S3H and Video 6). Additionally, K5 and K6A dynamics scores for K5^{high}/K6A^{high} cells were highly correlated, without evidence of bias between detection channels (Figure S3M). Taken together, these results establish a direct relationship between the mixture of keratin isoforms assembled into filaments and the dynamics of the networks that those filaments form.

The filament dynamics score is a composite measure of both intrinsic properties of the filaments, such as stiffness, and extrinsic interactions between the filament network and other cellular components, such as motor proteins. We reasoned that determining the portion of the keratin pro-

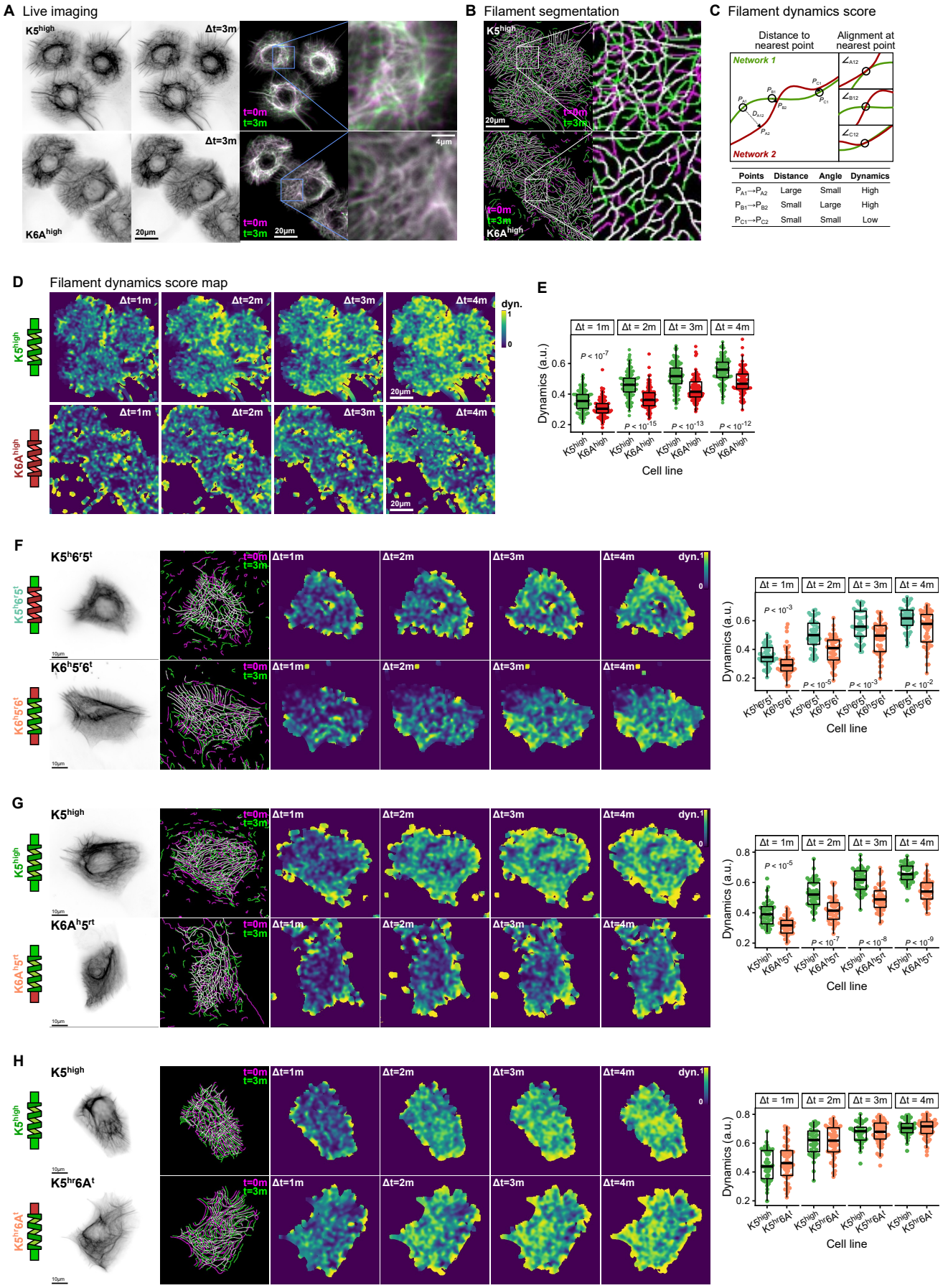
A Live imaging
B Filament segmentation
C Filament dynamics score
Distance to nearest point
Alignment at nearest point
Network 1
Network 2
Points | Distance | Angle | Dynamics
D Filament dynamics score map
E
Dynamics (a.u.)
Cell line
F
G
H

Previous page: **Figure 5. Wound-associated K6A alters keratin filament network dynamics.**

A. Keratin filaments in $K5^{high}$ and $K6A^{high}$ cells. Right, pseudo-color overlay of filament images captured 3 minutes apart.

B. Filament networks segmented using a computer vision pipeline (see Methods). As in (A), overlay of networks 3 minutes apart displays the dynamics of the network architecture. See also Video 6.

C. Schematic diagram of filament dynamics score calculation (see Methods).

D. Smoothed maps of local filament dynamics scores over different time intervals in $K5^{high}$ and $K6A^{high}$ cells.

E. Spatially averaged filament dynamics scores for each cell. *n* = 110-139 cells in 24-25 movies per group.

F. Comparison of filament dynamics scores between keratinocyte cell lines expressing high levels of chimeric keratins containing the head and tail domains of K5 or K6A joined to the rod domain of the opposite keratin ($K5^h6^r5^t$ and $K6^h5^r6^t$). *n* = 51-52 cells in 21-29 movies per group.

G-H. Comparison of filament dynamics scores between keratinocyte cell lines expressing high levels of chimeric keratins containing only the head (G; $K6A^h5^{rt}$) or tail (H; $K5^{hr}6A^t$) domains of K6A joined to the remainder of K5 with $K5^{high}$ cells. G, *n* = 44-47 cells in 28 movies per group. H, *n* = 45-60 cells in 37-39 movies per group.

tein responsible for the dynamics difference between $K5^{high}$ and $K6A^{high}$ filaments might begin to untangle these factors. Keratin proteins are composed of a central alpha helical rod domain flanked by intrinsically disordered head and tail domains[38,39]. To determine which domain was responsible for the difference in filament dynamics, we created chimeric keratin constructs composed of the head and tail domains of K5 or K6A fused to the rod domain from the opposite keratin ($K5^h6^r5^t$ and $K6^h5^r6^t$). Upon expressing each of these chimeras in cultured keratinocytes, we found that $K6^h5^r6^t$ decreased filament dynamics compared to $K5^h6^r5^t$ (Figure 5F). We further created chimeric keratins containing only the head or tail domain of K6A fused to the remainder of K5 ($K6A^h5^{rt}$ and $K5^{hr}6A^t$) and determined that the K6A head domain alone was sufficient to decrease filament dynamics (Figure 5G), while the K6A tail domain had no effect (Figure 5H). Thus, the intrinsically disordered K6A head domain, rather than the structural rod domain, is responsible for decreasing keratin filament dynamics.

Because the head domain has not been directly implicated in keratin filament structure[39], this result turned our attention to potential interactions between keratins and other cellular components. One such interaction implicates the actomyosin force-generating machinery, which could drive both keratin filament dynamics and cell migration. We reasoned that if a difference in actomyosin contractility was responsible for the difference between $K5^{high}$ and $K6A^{high}$ filament dynamics, inhibiting actomyosin contractility would reduce that effect. Indeed, we found that myosin inhibitor Blebbistatin completely eliminated the difference between $K5^{high}$ and $K6A^{high}$ filament dynamics (Figure S4A), while two upstream ROCK inhibitors had smaller effects (Figure S4B). This result led us to investigate potential interdependence between keratin filament composition and actomyosin force generation.

Wound-associated K6A increases cellular force generation by activating myosin

To directly test whether changing keratin filament composition affects cellular force generation, we compared the ability of $K5^{high}$ and $K6A^{high}$ cells to deform an elastic substrate using traction force microscopy[40]. We found that $K6A^{high}$ cells generated increased traction forces and strain energy compared to $K5^{high}$ cells (Figures 6A and S4C). Furthermore, this effect was reproduced by a cell line expressing the $K6A^h5^{rt}$ chimera (Figure 6B and S4D), indicating that, as with filament dynamics, traction force generation was modulated by differences in keratin head domains. Importantly, the increased strain energy, which measures the total work of contraction executed by the cell, cannot be explained by changes in mechanical properties such as filament elasticity or differences in organization of cell-matrix adhesions. This finding directly links shifts in the abundance of wound-associated K6A to cellular force generation.

Keratin filaments are not known to directly generate force. Rather, contractile forces are generated by myosin motor proteins linked to the actin cytoskeleton[41]. Non-muscle myosin activation occurs through phosphorylation of myosin regulatory light chain (pRLC)[42,43]. To directly compare pRLC between $K5^{high}$ and $K6A^{high}$ cells, we employed a proximity ligation assay, which uses two primary antibodies raised in different species, oligonucleotide-conjugated secondary antibodies, and rolling-circle amplification to detect colocalization between two antigens (Figure 6C)[44]. We probed for colocalization of myosin heavy chain (MYH9) and pRLC in a mosaic culture of $K5^{high}$ and $K6A^{high}$ keratinocytes. Consistent with the finding of increased contractility of $K6A^{high}$ cells, we measured increased colocalization of pRLC with MYH9, indicating increased myosin activation, in $K6A^{high}$ cells compared to $K5^{high}$ cells (Figure 6D).

We further probed for colocalization of pRLC with keratin filaments using either antibodies against K5 or K17. In both cases, we detected increased colocalizations in $K6A^{high}$ cells compared to $K5^{high}$ cells (Figure 6E-F), suggesting that myosin motors in the neighborhood of keratin filaments are more frequently activated when the relative amount of K6A is increased. Importantly, the colocalization between total regulatory light chain and K5 or K17 was similar or decreased in $K6A^{high}$ cells compared to $K5^{high}$ cells (Figure 6G-H), confirming that increased detection of pRLC near $K6A^{high}$ filaments reflects an increase in myosin activation, not merely a higher amount of total myosin near keratin filaments.

Keratin filament composition influences keratin filament-associated proteins

We next asked how changing keratin filament composition could alter myosin activation. We hypothesized that keratin filaments might serve as a platform to spatially organize components of a signaling pathway leading to RLC phosphorylation. If this was the case, changing keratin filament composition might alter the affinity of keratin filaments for components of such a signaling pathway, increasing or decreasing signal transduction. Reliable identification of keratin filament binding partners has been difficult for two reasons. First, keratins are expressed in extraordinary abun-

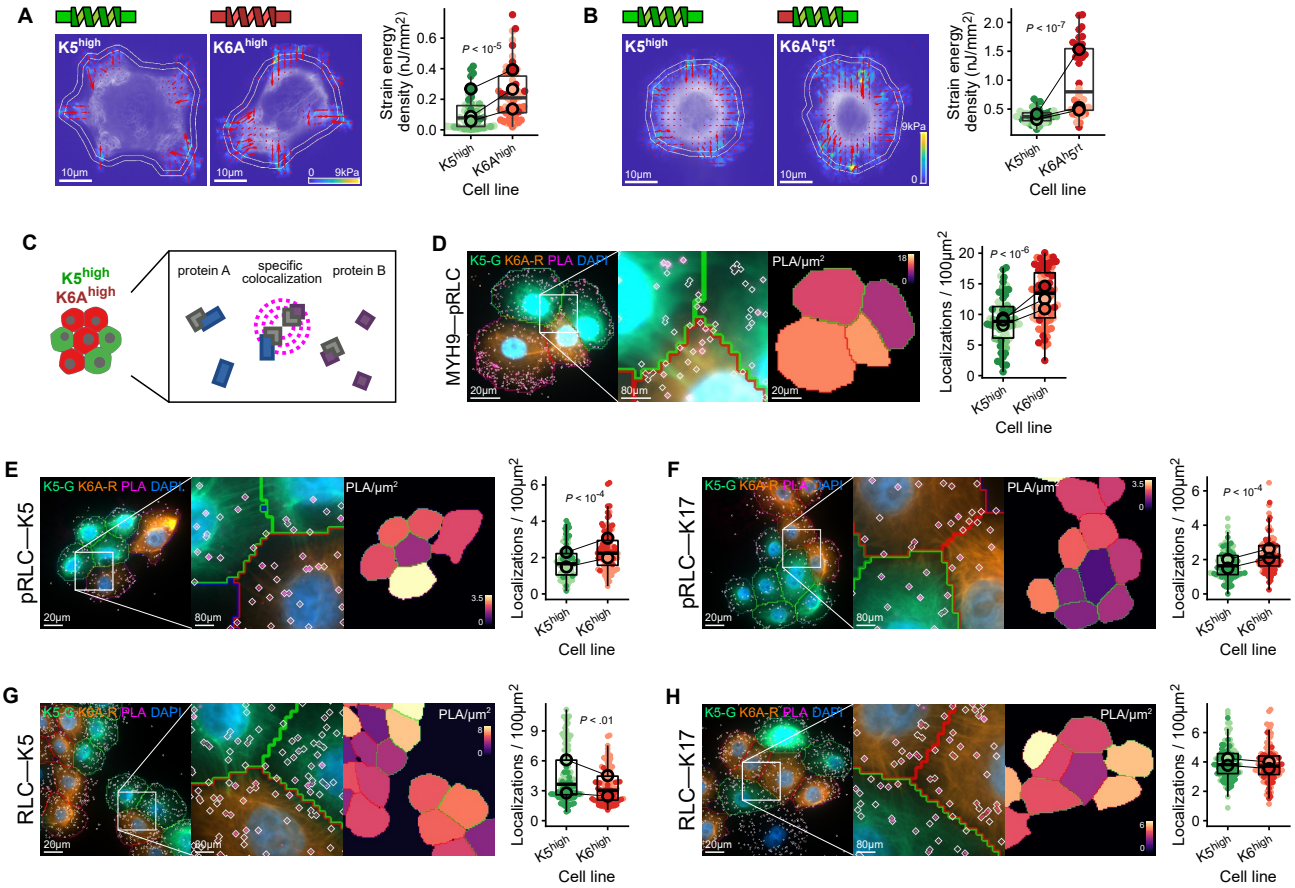

Figure 6. Wound-associated K6A increases cellular force generation by activating myosin.

A. Traction force microscopy (TFM) of K5^{high} and K6A^{high} cells (see Methods). Left, reconstructed traction vectors (arrows) on a heatmap of force magnitude and a watermark of keratin filament images (partially captured by the TIRF field). Inner ring, cell border based on keratin images; Outer ring, expanded boundary for strain energy calculation (see also Figure S4C). Right, strain energy density in K5^{high} and K6A^{high} cells. Outlined dots, connected between groups, mean values of experimental replicates in separate batches of TFM substrates. *n* = 51-58 cells per group.

B. TFM of cells expressing a chimeric keratin containing the head domain of K6A joined to the rod and tail of K5 (K6A^{h}5^{rt}) or full-length K5. See also Figure S4D. *n* = 40 cells per group.

C. Schematic diagram of the proximity ligation assay (PLA).

D. PLA detecting activated myosin by colocalization of phosphorylated myosin regulatory light chain (pRLC) and non-muscle myosin heavy chain (MYH9). Left, annotated images of K5^{high} (green outline) and K6A^{high} (red outline) cells. White diamonds, PLA detections (see Methods). Heatmap, PLA density (detections per 100 µm^2). K5-G, K5-mNeonGreen; K6A-R, K6A-mRuby2. Right, PLA detection density in K5^{high} and K6A^{high} cells. Outlined dots, connected between groups, mean values of experimental replicates. *n* = 66-80 cells per group in 37 total images.

E-F. PLA detecting activated myosin near keratin filaments by colocalization of pRLC and K5 (E) or K17 (F). E, *n* = 94-115 cells per group in 20 images. F, 99-108 cells per group in 23 images.

G-H. PLA detecting total myosin near keratin filaments by colocalization of total myosin regulatory light chain (RLC) and K5 (G) or K17 (H). G, *n* = 117-119 cells per group in 19 images. H, 121-129 cells per group in 21 images.

dance, representing about 30% of total protein in basal keratinocytes[45], which increases the risk of identifying non-specific associations. Second, epidermal keratin filaments are highly insoluble; the harsh, high-salt buffers capable of completely solubilizing keratin filaments likely disrupt interactions between keratins and other proteins[46]. While methods have been developed to immunoprecipitate epidermal keratins using milder detergents[46,47], it remains unclear if they reliably capture filamentous keratin versus soluble keratin monomers or smaller aggregates.

To overcome this challenge, we created keratinocyte cell lines expressing K5 or K6A fused to a promiscuous biotin ligase[48]. This allowed us to perform a proteomics screen comparing biotinylated proteins from each cell line[49], identifying in a differential manner proteins preferentially associated with keratin filaments in K5^{high} cells versus K6A^{high} cells (Figure 7A). These hits were implicated in a variety of functional processes, including cytoskeletal organization (Figure S5).

Wound-associated K6A recruits non-filamentous vimentin to keratin filaments

To our great surprise, among the proteins with overall high keratin filament association, vimentin showed the highest differential association between K6A^{high} and K5^{high} cells (Figure 7A-B). Vimentin, a type III intermediate filament protein, is the principal intermediate filament component in mesenchymal cells, and its expression in epithelial cells is associated with an epithelial to mesenchymal transition[50]. While vimentin expression is increased at migration edges in some non-keratinocyte[51,52] and cultured keratinocyte models[53,54], vimentin expression is not reliably induced in skin wounds where wound-induced keratin switching is clearly detectable (Figure 1B). Furthermore,

isoform-specific interactions between keratin filaments and vimentin have not previously been reported.

We first confirmed that our keratinocyte cell lines did express low levels of vimentin, with relatively increased vimentin in K6A^{high} cells compared to K5^{high} cells (Figure 7C). However, by immunofluorescence, vimentin filaments could be detected only in a very small fraction of keratinocytes (Figure S6). In this small minority of cells, vimentin filaments

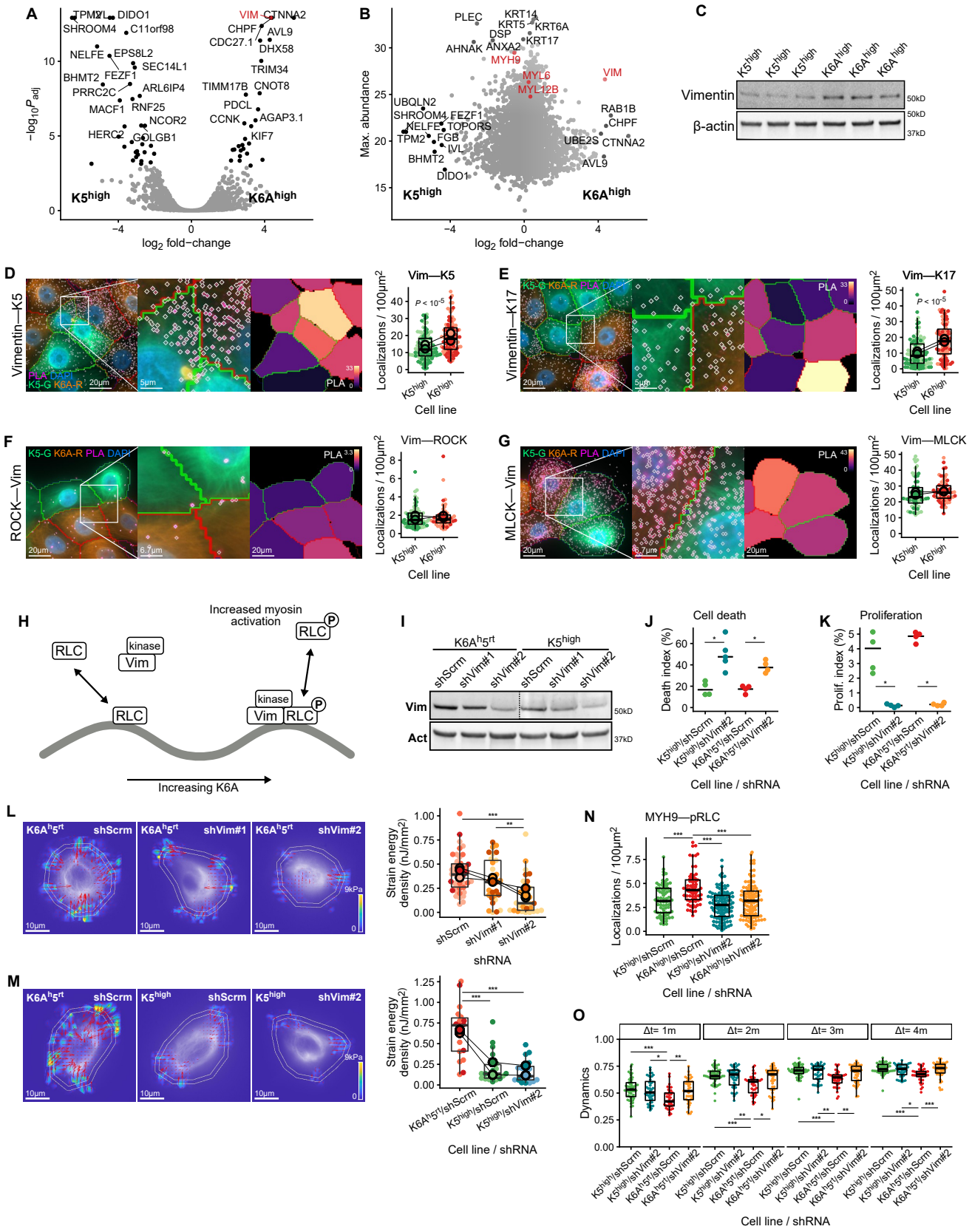

did not assemble into well-formed networks, but rather assembled into smaller aggregates or squiggles (Figure S6)[55]. The large majority of keratinocytes displayed no distinct vimentin structures at all, only a diffuse or speckled pattern (Figure S6). Vimentin filaments were somewhat more easily found at wound edges, (Figure S6A) but they could also be found in monolayer interiors (Figure S6B). Given the rarity of keratinocytes with vimentin filaments, we were not able to quantify their frequency precisely. However, there was no obvious difference in vimentin pattern between K5^{high} and K6A^{high} cells. Notably, when vimentin filaments were identified, they did not form along keratin filaments (Figure S6), and in some cases formed in a distinct vertical plane from the keratin filament network (Figure S6B).

Consistent with the proteomic screen, we identified increased association between vimentin and keratins in K6A^{high} cells compared to K5^{high} cells by a proximity ligation assay, regardless of whether K5 or K17 was used as the bait (Figure 7D-E). Furthermore, the increased association between vimentin and keratin filaments in K6A^{high} cells was a population effect, not driven by a small number of outlier cells which might represent those with vimentin filaments (Figures 7D-E and S6). Together, these data led us to the conclusion that a non-filamentous pool of vimentin interacts with keratin filaments, preferentially with the wound-associated keratin isoform K6A.

Non-filamentous vimentin shuttles myosin-activating kinases to K6A-contianing keratin filaments

How could association between non-filamentous vimentin and keratin promote actomyosin contractility through phosphorylation of myosin regulatory light chain? We considered the possibility that non-filamentous vimentin operates as a shuttle for kinases, bringing them into the proximity of keratin filaments, with a bias toward filaments with high K6A content. Vimentin was previously identified as a phosphorylation target for ROCK[56], which also targets RLC[57], implying at least transient ROCK-vimentin binding. While we detected only infrequent colocalization between vimentin and ROCK by proximity ligation (Figure 7F), we did detect frequent colocalization between vimentin and MLCK (Figure 7G), another RLC activator[42]. Neither ROCK nor MLCK were differentially associated with vimentin in K5^{high} compared to K6A^{high} cells (Figure 7F-G). However, once differentially shuttled to keratin filaments by vimentin, these kinases would be positioned near other keratin-associated proteins. Myosin subunits were previously shown to bind keratins[32], a finding recapitulated in our proteomics screen regardless of keratin isoform composition (Figure 7B). Thus, increasing the amount of K6A in keratin filaments would increase recruitment of regulatory kinases to activate myosin (Figure 7H).

This model implies a central role for vimentin mediating the activation of myosin and increased force generation with increased expression of wound-associated K6A. To test this, we knocked down vimentin in K5^{high} and K6A^{h}5^{rt} keratinocyte cell lines using lentiviral shRNA vectors (Figures 7I and S7A). Vimentin knockdown was poorly tolerated, with decreased proliferation and increased cell death within one week of shRNA expression (Figure 7J-K), consistent with previously reported findings in primary human keratinocytes[58,59]. Thus, we were unable to establish stable vimentin-depleted cell lines. However, by transient shRNA expression, we could perform traction force microscopy on vimentin knockdown keratinocytes and confirmed that vimentin depletion decreased traction force generation in K6A^{h}5^{rt} cells (Figure 7L). Vimentin depletion only slightly decreased traction force generation in K5^{high} cells, likely reflecting the lower baseline contractility of K5^{high} cells com-

Previous page: **Figure 7. Wound-associated K6A recruits non-filamentous vimentin, triggering myosin activation.**

A-B. Proteins differentially associated with keratin filaments in K5^{high} cells versus K6A^{high} cells were identified by proximity biotinylation, streptavidin pulldown, and mass spectrometry (see Methods). A, Volcano plot highlighting differentially associated proteins. B, Differential association compared to the maximum protein abundance across all samples. n = 2 samples per group.

C. Western blot analysis of vimentin expression in K5^{high} and K6A^{high} cells. See also Figure S1B for additional blots with these samples; β-actin control repeated for reference.

D-E. Proximity ligation assay (PLA) detecting colocalization between vimentin and K5 (D) or K17 (E). Left, annotated images of K5^{high} (green outline) and K6A^{high} (red outline) cells. White diamonds, PLA detections. Heatmap, PLA density (detections per 100 μm^2). K5-G, K5-mNeonGreen; K6A-R, K6A-mRuby2. Right, PLA detection density in K5^{high} and K6A^{high} cells. Outlined dots, connected between groups, mean values of experimental replicates. D, n = 103-113 cells per group in 17 images. E, n = 84-105 cells per group in 18 images.

F-G. PLA detecting colocalization between vimentin and ROCK (F) or MLCK (G). Left, annotated images as in (D-E). Right, PLA detection density. Outlined dots, connected between groups, mean values of experimental replicates. Note the different ranges in (F) and (G). F, n = 87-121 cells per group in 20 images. G, n = 80-105 cells per group in 19 images.

H. Schematic diagram of the proposed model. Non-filamentous vimentin (Vim) shuttles regulatory kinases preferentially to K6A-containing filaments, where they phosphorylate myosin regulatory light chain.

I. Western blot analysis of vimentin knockdown by shRNA (shVim#1; shVim#2; scrambled control, shScrm) in keratinocytes expressing a chimeric keratin containing the head domain of K6A joined to the rod and tail of K5 (K6A^{h}5^{rt}) or full-length K5 (K5^{high}). Dashed line separates different brightness adjustments for different baseline vimentin levels. See also Figure S7A for an alternate display.

J. Death of K5^{high} and K6A^{h}5^{rt} cells upon expression of shVim#2 versus shScrm. Cell death index, percentage of nuclei with membrane-impermeable DNA dye uptake (see Methods). *, P < .05. n = 4-5 samples with 112-162 total cells per group.

K. Proliferation of K5^{high} and K6A^{h}5^{rt} cells upon expression of shVim#2 versus shScrm. Proliferation index, percentage of cells with EdU uptake (see Methods). *, P < .05. n = 4 samples with 2,897-6,013 total cells per group.

L-M. Traction force microscopy (TFM) of K6A^{h}5^{rt} or K5^{high} cells upon expression of shVim#1, shVim#2, or shScrm. Left, reconstructed traction force vectors (arrows) on a heatmap of force magnitude and a watermark of keratin filament images. Inner ring, cell border based on keratin images. Outer ring, expanded boundary used for strain energy calculation. Right, comparison of strain energy densities between treatment groups. Outlined dots, connected between groups, mean values of experimental replicates in separate batches of TFM substrates. ***, P < 10^{-3}; **, P < .01. L, n = 29-43 cells per group. M, n = 18-21 cells per group.

N. PLA detecting myosin activation by colocalization of phosphorylated myosin regulatory light chain (pRLC) and non-muscle myosin heavy chain (MYH9) in K6A^{high} and K5^{high} cells upon expression of shVim#2 or shScrm. See also annotated images in Figure S9B. ***, P < 10^{-3}. n = 67-113 cells per group in 16-24 images per shRNA condition.

O. Keratin filament network dynamics in K6A^{h}5^{rt} cells and K5^{high} cells upon expression of shVim#2 or shScrm. See also Figure S10 for filament images, segmentations, and dynamics score maps. ***, P < 10^{-3}; **, P < .01; *, P < .05. n = 39-49 cells per group.

pared to K6A^{h}5^{rt} cells (Figure 7M). Consistent with this, vimentin knockdown decreased myosin activation in K6A^{high} cells to a level similar to that of K5^{high} cells (Figures 7N and S7B). Furthermore, vimentin knockdown reversed the effect of K6A on keratin filament dynamics. Compared to a scrambled shRNA control, vimentin shRNA increased filament dynamics in K6A^{h}5^{rt} cells nearly to the level seen in K5^{high} cells (Figures 7O and S7C). Filament dynamics were little changed by vimentin knockdown in K5^{high} cells (Figures 7O and S7C). Altogether, these results show that increased traction force generation and decreased filament dynamics caused by wound-associated K6A both depend on the non-filamentous vimentin pool acting as a shuttle for kinases.

Discussion

Our data reveal an unexpected role for keratin filaments as signaling scaffolds in addition to their canonical role as mechanical scaffolds. Increasing expression of wound-associated K6A supports epidermal remodeling not by altering the cell's mechanical capacity for force resistance, but by organizing molecular signals that activate force generation to drive migration. This signal transduction cascade relies on an isoform-preferential interaction between the intrinsically disordered K6A head domain and non-filamentous vimentin shuttling myosin activating kinases. As the amount of K6A incorporated into keratin filaments increases, more kinase is shuttled to keratin filaments where it phosphorylates nearby RLC, leading to myosin activation.

The proposed pathway establishes functional coupling between the cellular machinery of force resistance and force generation during epidermal remodeling, exactly the context where the balance between epidermal stability and plasticity needs to shift. Importantly, keratin isoform switching modulates signaling scaffold function without disrupting mechanical scaffold function. During wound healing, the epidermis remains subject to mechanical stress, both from the usual external insults and directly resulting from tissue remodeling, so the keratin mechanical scaffold remains essential. Our finding that increased K6A expression does not impair epidermal stability fits with this requirement, as do prior studies demonstrating increased keratinocyte fragility during wound healing when all K6 isoforms are deleted[18,31].

Increased cellular force generation necessarily increases cell exposure to mechanical stress. Thus, the ability of keratins to functionally couple force resistance and force generation could be broadly important. One possibility is that an actomyosin-activating signaling cascade dependent on keratin filaments restricts force generation in cells lacking a keratin filament network sufficient to maintain structural integrity under stress. A second intriguing hypothesis comes from our seemingly paradoxical observation that elevated K6A expression decreases intracellular movement of keratin filaments yet increases force generation. We offer as a plausible explanation that non-filamentous vimentin acts not only as a kinase shuttle, but also as a cytoplasmic glue, sticking keratin filaments to other cellular components such as actomyosin stress fibers[60,61], thus decreasing K6A-enriched keratin filament dynamics under a given force. Wound-associated keratins might then function both to activate actomyosin contractility and to stabilize otherwise brittle actin structures[62]. Expansive additional investigation will be needed to evaluate these possibilities.

Our results also highlight an underappreciated role of vimentin in epithelial tissues. In contexts such as development and cancer metastasis, vimentin expression is a marker of epithelial to mesenchymal transition (EMT)[63], but in stable epithelia vimentin has been thought to be irrelevant. Wound healing can be considered a reversible forme fruste of EMT[63], and defective wound healing is among the most prominent phenotypes of a vimentin knock-out mouse[64]. Although this has been attributed to defects in dermal fibroblasts[65], our results suggest that the keratinocytes themselves may significantly contribute to the phenotype because of their dependence on vimentin as a shuttle for molecular signals. Furthermore, our finding that vimentin knockdown compromises keratinocyte growth in culture despite the absence of vimentin filaments, consistent with previously reported findings[58,59], underscores the importance of non-filamentous vimentin[66] for cellular homeostasis, even in epithelial cells.

Given the intricate pattern of keratin isoform expression depending on tissue, anatomic site, and differentiation state[3], keratin isoform differences are very likely to support signal transduction cascades in additional contexts. Notably, the structural rod domain is highly conserved between keratin isoforms, suggesting little opportunity to influence the mechanical scaffold[38]. However, the intrinsically disordered head and tail domains are highly variable between isoforms[38]. Recent reports that intermediate filament head and tail domains interact through labile cross-β-strand polymerization establish a thus far undiscussed potential for cell regulation through complex interaction networks between the intermediate filament cytoskeleton and other cytoplasmic proteins and subcellular structures[67,68]. Such interactions could allow intermediate filaments to spatiotemporally organize a variety of biochemical processes, akin to the signaling pathway leading to actomyosin activation by wound-associated K6A identified here. Thus, this study sets the stage for investigations of the diversity of intermediate filament interactions as a new regulatory motif in the adaptive control of cell function.

Acknowledgements

We thank Kim Reed and other members of the Danuser laboratory for technical support and helpful discussion; Jerry Shay, Kimberly Batten, Richard Wang and Travis Vandergriff for reagents and advice; John Shelton, Diana Wigginton, and Cameron Perry from the UT Southwestern Histo Pathology Core for histology services and technical support; the Moody Foundation Flow Cytometry Facility of the Children's Medical Center Research Institute at UT Southwestern; the UT Southwestern Flow and Mass Cytometry Facility; the UT Southwestern Electron Microscopy Core Facility, supported in part by the National Institutes of Health (S10OD021685); the UT Southwestern Proteomics Core Facility; and the BioHPC computing facility at UT Southwestern. B.A.N. is supported by a Career Development Award from the Dermatology Foundation, the National Institutes of Health (T32AR065969), and the UT Southwestern Physician Scientist Training Program. Research in the Danuser lab is supported by a grant from the

National Institute of General Medical Sciences (R35GM136428).

References

1 Gonzales, K. A. U. & Fuchs, E. Skin and Its Regenerative Powers: An Alliance between Stem Cells and Their Niche. *Dev Cell* **43**, 387-401 (2017). https://doi.org:10.1016/j.devcel.2017.10.001

2 Hatzfeld, M., Keil, R. & Magin, T. M. Desmosomes and Intermediate Filaments: Their Consequences for Tissue Mechanics. *Cold Spring Harb Perspect Biol* **9** (2017). https://doi.org:10.1101/cshperspect.a029157

3 Moll, R., Divo, M. & Langbein, L. The human keratins: biology and pathology. *Histochem Cell Biol* **129**, 705-733 (2008). https://doi.org:10.1007/s00418-008-0435-6

4 Toivola, D. M., Boor, P., Alam, C. & Strnad, P. Keratins in health and disease. *Curr Opin Cell Biol* **32**, 73-81 (2015). https://doi.org:10.1016/j.ceb.2014.12.008

5 Shaw, T. J. & Martin, P. Wound repair at a glance. *J Cell Sci* **122**, 3209-3213 (2009). https://doi.org:10.1242/jcs.031187

6 Iizuka, H., Takahashi, H. & Ishida-Yamamoto, A. Psoriatic architecture constructed by epidermal remodeling. *J Dermatol Sci* **35**, 93-99 (2004). https://doi.org:10.1016/j.jdermsci.2004.01.003

7 Hanahan, D. & Weinberg, R. A. Hallmarks of cancer: the next generation. *Cell* **144**, 646-674 (2011). https://doi.org:10.1016/j.cell.2011.02.013

8 Weiss, R. A., Eichner, R. & Sun, T. T. Monoclonal antibody analysis of keratin expression in epidermal diseases: a 48- and 56-kdalton keratin as molecular markers for hyperproliferative keratinocytes. *J Cell Biol* **98**, 1397-1406 (1984). https://doi.org:10.1083/jcb.98.4.1397

9 Mansbridge, J. N. & Knapp, A. M. Changes in keratinocyte maturation during wound healing. *J Invest Dermatol* **89**, 253-263 (1987). https://doi.org:10.1111/1523-1747.ep12471216

10 Patel, G. K., Wilson, C. H., Harding, K. G., Finlay, A. Y. & Bowden, P. E. Numerous keratinocyte subtypes involved in wound re-epithelialization. *J Invest Dermatol* **126**, 497-502 (2006). https://doi.org:10.1038/sj.jid.5700101

11 Esgleyes-Ribot, T., Chandraratna, R. A., Lew-Kaya, D. A., Sefton, J. & Duvic, M. Response of psoriasis to a new topical retinoid, AGN 190168. *J Am Acad Dermatol* **30**, 581-590 (1994). https://doi.org:10.1016/s0190-9622(94)70066-4

12 Duvic, M., Nagpal, S., Asano, A. T. & Chandraratna, R. A. Molecular mechanisms of tazarotene action in psoriasis. *J Am Acad Dermatol* **37**, S18-24 (1997).

13 Hameetman, L. *et al.* Molecular profiling of cutaneous squamous cell carcinomas and actinic keratoses from organ transplant recipients. *BMC Cancer* **13**, 58 (2013). https://doi.org:10.1186/1471-2407-13-58

14 Machesney, M., Tidman, N., Waseem, A., Kirby, L. & Leigh, I. Activated keratinocytes in the epidermis of hypertrophic scars. *Am J Pathol* **152**, 1133-1141 (1998).

15 Aragona, M. *et al.* Mechanisms of stretch-mediated skin expansion at single-cell resolution. *Nature* (2020). https://doi.org:10.1038/s41586-020-2555-7

16 Vassar, R., Coulombe, P. A., Degenstein, L., Albers, K. & Fuchs, E. Mutant keratin expression in transgenic mice causes marked abnormalities resembling a human genetic skin disease. *Cell* **64**, 365-380 (1991). https://doi.org:10.1016/0092-8674(91)90645-f

17 Wojcik, S. M., Bundman, D. S. & Roop, D. R. Delayed wound healing in keratin 6a knockout mice. *Mol Cell Biol* **20**, 5248-5255 (2000). https://doi.org:10.1128/mcb.20.14.5248-5255.2000

18 Wong, P. *et al.* Introducing a null mutation in the mouse K6alpha and K6beta genes reveals their essential structural role in the oral mucosa. *J Cell Biol* **150**, 921-928 (2000). https://doi.org:10.1083/jcb.150.4.921

19 Lessard, J. C. *et al.* Keratin 16 regulates innate immunity in response to epidermal barrier breach. *Proc Natl Acad Sci U S A* **110**, 19537-19542 (2013). https://doi.org:10.1073/pnas.1309576110

20 McGowan, K. M. *et al.* Keratin 17 null mice exhibit age- and strain-dependent alopecia. *Genes Dev* **16**, 1412-1422 (2002). https://doi.org:10.1101/gad.979502

21 Wojcik, S. M., Longley, M. A. & Roop, D. R. Discovery of a novel murine keratin 6 (K6) isoform explains the absence of hair and nail defects in mice deficient for K6a and K6b. *J Cell Biol* **154**, 619-630 (2001). https://doi.org:10.1083/jcb.200102079

22 Zieman, A. G. & Coulombe, P. A. Pathophysiology of pachyonychia congenita-associated palmoplantar keratoderma: new insights into skin epithelial homeostasis and avenues for treatment. *Br J Dermatol* (2019). https://doi.org:10.1111/bjd.18033

23 Wu, T. T., Eldirany, S. A., Bunick, C. G. & Teng, J. M. C. Genotype–Structurotype–Phenotype Correlations in Patients with Pachyonychia Congenita. *J Invest Dermatol* **141**, 2876-2884 e2874 (2021). https://doi.org:10.1016/j.jid.2021.03.035

24 Iglesias-Bartolome, R. *et al.* Transcriptional signature primes human oral mucosa for rapid wound healing. *Sci Transl Med* **10** (2018). https://doi.org:10.1126/scitranslmed.aap8798

25 Ramirez, H. A. *et al.* Staphylococcus aureus Triggers Induction of miR-15B-5P to Diminish DNA Repair and Deregulate Inflammatory Response in Diabetic Foot Ulcers. *J Invest Dermatol* **138**, 1187-1196 (2018). https://doi.org:10.1016/j.jid.2017.11.038

26 Boukamp, P. *et al.* Normal keratinization in a spontaneously immortalized aneuploid human keratinocyte cell line. *J Cell Biol* **106**, 761-771 (1988). https://doi.org:10.1083/jcb.106.3.761

27 Leigh, I. M. *et al.* Keratins (K16 and K17) as markers of keratinocyte hyperproliferation in psoriasis in vivo and in vitro. *Br J Dermatol* **133**, 501-511 (1995). https://doi.org:10.1111/j.1365-2133.1995.tb02696.x

28 Ramirez, R. D. *et al.* Bypass of telomere-dependent replicative senescence (M1) upon overexpression of Cdk4 in normal human epithelial cells. *Oncogene* **22**, 433-444 (2003). https://doi.org:10.1038/sj.onc.1206046

29 Vaughan, M. B., Ramirez, R. D., Andrews, C. M., Wright, W. E. & Shay, J. W. H-ras expression in immortalized keratinocytes produces an invasive epithelium in cultured skin equivalents. *PLoS One* **4**, e7908 (2009). https://doi.org:10.1371/journal.pone.0007908

30 Simpson, C. L., Patel, D. M. & Green, K. J. Deconstructing the skin: cytoarchitectural determinants of epidermal morphogenesis. *Nat Rev Mol Cell Biol* **12**, 565-580 (2011). https://doi.org:10.1038/nrm3175

31 Wong, P. & Coulombe, P. A. Loss of keratin 6 (K6) proteins reveals a function for intermediate filaments during wound repair. *J Cell Biol* **163**, 327-337 (2003). https://doi.org:10.1083/jcb.200305032

32 Wang, F., Chen, S., Liu, H. B., Parent, C. A. & Coulombe, P. A. Keratin 6 regulates collective keratinocyte migration by altering cell-cell and cell-matrix adhesion. *J Cell Biol* **217**, 4314-4330 (2018). https://doi.org:10.1083/jcb.201712130

33 Seltmann, K. *et al.* Keratins mediate localization of hemidesmosomes and repress cell motility. *J Invest Dermatol* **133**, 181-190 (2013). https://doi.org:10.1038/jid.2012.256

34 Kroger, C. *et al.* Keratins control intercellular adhesion involving PKC-alpha-mediated desmoplakin phosphorylation. *J Cell Biol* **201**, 681-692 (2013). https://doi.org:10.1083/jcb.201208162

35 Zaritsky, A. *et al.* Diverse roles of guanine nucleotide exchange factors in regulating collective cell migration. *J Cell Biol* **216**, 1543-1556 (2017). https://doi.org:10.1083/jcb.201609095

36 Gan, Z. *et al.* Vimentin Intermediate Filaments Template Microtubule Networks to Enhance Persistence in Cell Polarity and Directed Migration. *Cell Syst* **3**, 252-263 e258 (2016). https://doi.org:10.1016/j.cels.2016.08.007

37 Paramio, J. M., Casanova, M. L., Alonso, A. & Jorcano, J. L. Keratin intermediate filament dynamics in cell heterokaryons reveals diverse behaviour of different keratins. *J Cell Sci* **110 (Pt 9)**, 1099-1111 (1997).

38 Eldirany, S. A., Lomakin, I. B., Ho, M. & Bunick, C. G. Recent insight into intermediate filament structure. *Curr Opin Cell Biol* **68**, 132-143 (2020). https://doi.org:10.1016/j.ceb.2020.10.001

39 Herrmann, H. & Aebi, U. Intermediate Filaments: Structure and Assembly. *Cold Spring Harb Perspect Biol* **8** (2016). https://doi.org:10.1101/cshperspect.a018242

40 Han, S. J., Oak, Y., Groisman, A. & Danuser, G. Traction microscopy to identify force modulation in subresolution adhesions. *Nature methods* **12**, 653-656 (2015). https://doi.org:10.1038/nmeth.3430

41 van Bodegraven, E. J. & Etienne-Manneville, S. Intermediate filaments against actomyosin: the david and goliath of cell migration. *Curr Opin Cell Biol* **66**, 79-88 (2020). https://doi.org:10.1016/j.ceb.2020.05.006

42 Scholey, J. M., Taylor, K. A. & Kendrick-Jones, J. Regulation of non-muscle myosin assembly by calmodulin-dependent light chain kinase. *Nature* **287**, 233-235 (1980). https://doi.org:10.1038/287233a0

43 Brito, C. & Sousa, S. Non-Muscle Myosin 2A (NM2A): Structure, Regulation and Function. *Cells* **9** (2020). https://doi.org:10.3390/cells9071590

44 Fredriksson, S. *et al.* Protein detection using proximity-dependent DNA ligation assays. *Nat Biotechnol* **20**, 473-477 (2002). https://doi.org:10.1038/nbt0502-473

45 Sun, T. T. & Green, H. Keratin filaments of cultured human epidermal cells. Formation of intermolecular disulfide bonds during terminal differentiation. *J Biol Chem* **253**, 2053-2060 (1978).

46 Wang, F., Zieman, A. & Coulombe, P. A. Skin Keratins. *Methods Enzymol* **568**, 303-350 (2016). https://doi.org:10.1016/bs.mie.2015.09.032

47 Lowthert, L. A., Ku, N. O., Liao, J., Coulombe, P. A. & Omary, M. B. Empigen BB: a useful detergent for solubilization and biochemical analysis of keratins. *Biochem Biophys Res Commun* **206**, 370-379 (1995). https://doi.org:10.1006/bbrc.1995.1051

48 Branon, T. C. *et al.* Efficient proximity labeling in living cells and organisms with TurboID. *Nat Biotechnol* **36**, 880-887 (2018). https://doi.org:10.1038/nbt.4201

49 Cable, C. J., Kaplan, N., Getsios, S., Thomas, P. M. & Perez White, B. E. Biotin Identification Proteomics in Three-Dimensional Organotypic Human Skin Cultures. *Methods in molecular biology* (2019). https://doi.org:10.1007/7651_2019_239

50 Oshima, R. G. Intermediate filaments: a historical perspective. *Exp Cell Res* **313**, 1981-1994 (2007). https://doi.org:10.1016/j.yexcr.2007.04.007

51 Gilles, C. *et al.* Vimentin contributes to human mammary epithelial cell migration. *J Cell Sci* **112 (Pt 24)**, 4615-4625 (1999).

52 Menko, A. S. *et al.* A central role for vimentin in regulating repair function during healing of the lens epithelium. *Mol Biol Cell* **25**, 776-790 (2014). https://doi.org:10.1091/mbc.E12-12-0900

53 Takada, K. *et al.* Poly I:C induces collective migration of HaCaT keratinocytes via IL-8. *BMC Immunol* **18**, 19 (2017). https://doi.org:10.1186/s12865-017-0202-3

54 Biddle, D. & Spandau, D. F. Expression of vimentin in cultured human keratinocytes is associated with cell - extracellular matrix junctions. *Arch Dermatol Res* **288**, 621-624 (1996). https://doi.org:10.1007/BF02505266

55 Yoon, M., Moir, R. D., Prahlad, V. & Goldman, R. D. Motile properties of vimentin intermediate filament networks in living cells. *J Cell Biol* **143**, 147-157 (1998). https://doi.org:10.1083/jcb.143.1.147

56 Goto, H. *et al.* Phosphorylation of vimentin by Rho-associated kinase at a unique amino-terminal site that is specifically phosphorylated during cytokinesis. *J Biol Chem* **273**, 11728-11736 (1998). https://doi.org:10.1074/jbc.273.19.11728

57 Sellers, J. R., Pato, M. D. & Adelstein, R. S. Reversible phosphorylation of smooth muscle myosin, heavy meromyosin, and platelet myosin. *J Biol Chem* **256**, 13137-13142 (1981).

58 Castro-Munozledo, F., Velez-DelValle, C., Marsch-Moreno, M., Hernandez-Quintero, M. & Kuri-Harcuch, W. Vimentin is necessary for colony

growth of human diploid keratinocytes. *Histochem Cell Biol* **143**, 45-57 (2015). https://doi.org:10.1007/s00418-014-1262-6
59 Velez-delValle, C., Marsch-Moreno, M., Castro-Munozledo, F., Galvan-Mendoza, I. J. & Kuri-Harcuch, W. Epithelial cell migration requires the interaction between the vimentin and keratin intermediate filaments. *Sci Rep* **6**, 24389 (2016). https://doi.org:10.1038/srep24389
60 Green, K. J., Geiger, B., Jones, J. C., Talian, J. C. & Goldman, R. D. The relationship between intermediate filaments and microfilaments before and during the formation of desmosomes and adherens-type junctions in mouse epidermal keratinocytes. *J Cell Biol* **104**, 1389-1402 (1987). https://doi.org:10.1083/jcb.104.5.1389
61 Esue, O., Carson, A. A., Tseng, Y. & Wirtz, D. A direct interaction between actin and vimentin filaments mediated by the tail domain of vimentin. *J Biol Chem* **281**, 30393-30399 (2006). https://doi.org:10.1074/jbc.M605452200
62 Pegoraro, A. F., Janmey, P. & Weitz, D. A. Mechanical Properties of the Cytoskeleton and Cells. *Cold Spring Harb Perspect Biol* **9** (2017). https://doi.org:10.1101/cshperspect.a022038
63 Nakamura, M. & Tokura, Y. Epithelial-mesenchymal transition in the skin. *J Dermatol Sci* **61**, 7-13 (2011). https://doi.org:10.1016/j.jdermsci.2010.11.015
64 Eckes, B. *et al.* Impaired wound healing in embryonic and adult mice lacking vimentin. *J Cell Sci* **113 (Pt 13)**, 2455-2462 (2000).
65 Cheng, F. *et al.* Vimentin coordinates fibroblast proliferation and keratinocyte differentiation in wound healing via TGF-beta-Slug signaling. *Proc Natl Acad Sci U S A* **113**, E4320-4327 (2016). https://doi.org:10.1073/pnas.1519197113
66 Soellner, P., Quinlan, R. A. & Franke, W. W. Identification of a distinct soluble subunit of an intermediate filament protein: tetrameric vimentin from living cells. *Proc Natl Acad Sci U S A* **82**, 7929-7933 (1985). https://doi.org:10.1073/pnas.82.23.7929
67 Zhou, X. *et al.* Transiently structured head domains control intermediate filament assembly. *Proc Natl Acad Sci U S A* **118** (2021). https://doi.org:10.1073/pnas.2022121118
68 Lin, Y. *et al.* Toxic PR Poly-Dipeptides Encoded by the C9orf72 Repeat Expansion Target LC Domain Polymers. *Cell* **167**, 789-802 e712 (2016). https://doi.org:10.1016/j.cell.2016.10.003

Methods

Cell culture

Human keratinocyte Ker-CT cells (ATCC #CRL-4048) were a kind gift from Dr. Jerry Shay (UT Southwestern Medical Center). This cell line was developed from human foreskin keratinocytes through expression of HTERT and CDK4 [1,2]. Unless otherwise specified, keratinocytes were cultured on tissue-culture treated plastic coated with bovine type I collagen (PureCol, Advanced Biomatrix #5005) by pre-incubating dishes in a 100 µg/mL collagen solution for 30 minutes. Cells were maintained in Keratinocyte serum-free medium (K-SFM; Gibco #17005042) with the included 5 ng/mL human recombinant epidermal growth factor and 50 mg/mL bovine pituitary extract supplements according to the manufacturer's instructions in a humidified incubator at 37 °C and 5% CO_2. K-SFM contains a low calcium concentration which supports keratinocyte growth without inducing differentiation, but which also limits desmosome formation[3]. To induce desmosome formation and support differentiation for certain experiments, we developed a keratinocyte differentiation medium based on a simplification of the classic Rheinwald and Green formula[4,5]. This medium was composed of fully-supplemented K-SFM mixed in equal parts with DMEM/F12 (Gibco #11320033) and additionally supplemented with 2% fetal bovine serum (Sigma F0926). HEK293 cells (a gift from H. Choe) used for generation of lentiviral particles were maintained in DMEM (Gibco #11995-065) supplemented with 10% fetal bovine serum (Sigma F0926) and antibiotic–antimycotic reagent (Gibco #15240-062) in a humidified incubator at 37 °C and 5% CO_2. All cell lines were periodically tested for mycoplasma using a PCR-based Genlantis Mycoscope Detection Kit (MY01100).

Plasmids

Primer and synthetic DNA sequences (Integrated DNA Technologies) used to assemble the following constructs are provided in Table S1.

Keratin sequences were cloned by polymerase chain reaction (PCR) from pBabe-RFP1-KRT5-hygro (Addgene #58493) and pDONR22-KRT6A (DNASU clone HsCD00039474) and inserted into pLVX-IRES-Puro or pLVX-IRES-Neo lentiviral expression vectors (Clontech) with C-terminal fluorescent tags using seamless cloning (HiFi DNA Assembly Master Mix, New England Biolabs). The pLVX-KRT5-mNG-IRES-Puro construct includes an mNeonGreen (Allele Biotechnology)[6] sequence in-frame with the KRT5 sequence separated by a short peptide linker (DPAFLY). Similarly, the pLVX-KRT6A-mRb-IRES-Neo construct includes an mRuby2 (Addgene #40260)[7] sequence in-frame with the KRT6A sequence separated by the same linker.

Keratin head/tail domain chimera constructs were assembled using seamless cloning into pLVX-IRES-Puro, with keratin domains cloned from the above pLVX-KRT5-mNG-IRES-Puro and pLVX-KRT6A-mRb-IRES-Neo constructs by PCR. Keratin domains were defined based on NCBI Reference Sequence annotations (NP_000415.2, NP_005545.1). Specifically, the K5 head and tail domains included amino acids 1-167 and 478-590 respectively; the K6A head and tail domains included amino acids 1-162 and 473-564 respectively.

For proximity biotin labeling experiments, the sequence of miniTurbo, a small promiscuous biotin ligase[8], was synthesized with a C-terminal Flag tag and flanking XbaI and BamHI restriction sites. This fragment was then inserted into pLVX-IRES-Puro using the XbaI and BamHI sites. Finally, the KRT5 and KRT6A sequences were amplified by PCR from the above pLVX-KRT5-mNG-IRES-Puro and pLVX-KRT6A-mRb-IRES-Neo constructs and inserted in-frame and N-terminal to the biotin ligase with a short peptide linker (DPAFSR) using seamless cloning. To create a marker construct for these experiments, EGFP from pEGFP-C1 (Clontech) was inserted into pLVX-IRES-Puro using the SnaBI and BamHI restriction sites.

For shRNA experiments, pLKO.1-Scrambled (Addgene #136035)[9] was modified to express H2B-mRuby3 for visual identification of transduced cells based on a nuclear fluorescence signal[10]. The H2B-mRuby3 sequence was synthesized and inserted into pLKO.1 in place of the existing PuroR sequence using BamHI and KpnI restriction sites. Vimentin targeting sequences for shRNA constructs were selected from the Genetic Perturbation Platform Web Portal (Broad Institute; https://portals.broadinstitute.org/gpp/). Complementary primers were synthesized and annealed, then cloned into pLKO1-H2B-mRuby3 using AgeI and EcoRI restriction sites. The clones selected for shVim#1 (TRCN0000029120) and shVim#2 (TRCN0000029119) have, respectively, moderate and high predicted knockdown performance.

Lentivirus transduction and cell line selection

Lentiviral particles were generated using the pLVX system (Clontech) with packaging vectors psPAX2 and pMD2.G (Addgene plasmids #12260 and #12259). HEK293 cells were transfected with expression and packing plasmids following standard calcium phosphate or polyethylenimine (Polysciences #23966) protocols. Supernatant was collected two days after transfection, filtered through 0.45-µm mixed cellulose esters membrane syringe filters (Fisher Scientific #09-720-005) and incubated on target cells overnight. After multiple days of culture and cell expansion, cells expressing the relevant fluorescent marker were collected on FACS Aria II SORP flow cytometer equipped with 405 nm, 488 nm, 561 nm, and 633 nm lasers (Beckton Dickinson) and returned to culture.

Western blotting

Cells were grown to confluence and switched to differentiation medium 24 hours prior to sample collection. Because keratin filaments are highly insoluble, a high-ionic-strength urea buffer was used in place of a standard lysis buffer[11]. The 6.5 M urea lysis buffer also contained 50 mM tris, 1 mM EGTA, 2 mM DTT, 50 mM sodium fluoride, 1 mM sodium vanadate, and Halt Protease Inhibitor Cocktail (ThermoFisher #78430), and was adjusted to pH 7.5. After washing twice with PBS, cells were collected into urea lysis buffer using a cell scraper, then incubated at 4 °C for 20 minutes on a shaker. The lysates were then sonicated using a Fisherbrand Model 505 Sonic Dismembrator (ThermoFisher) twice for 10 seconds at 20% power with a 10 second intervening rest. Any remaining insoluble material was pelleted by centrifugation at 16.1×10^3 *g* for 20 minutes at 4 °C, and the supernatant was transferred to a clean tube. Protein concentrations were measured using a BCA assay (ThermoFisher #23228). Laemmli sample buffer (BioRad #161-0747) with 2-mercaptoethanol (ThermoFisher #BP176) was added to the samples, which were then heated to 95 °C for 5 minutes.

Samples were run on 4-20% Mini-PROTEAN pre-cast gels (Biorad) and transferred to nitrocellulose membranes (ThermoFisher #88018). Once membranes were blocked with 5% bovine serum albumin (BSA; Equitech-Bio BAH65-0500) in Tris buffered saline (TBS) with 0.1% Tween 20 (TBST; ThermoFisher BP337) for 1 hour at room temperature, they were incubated in primary antibodies overnight at 4 °C (Table S2). Membranes were washed with TBST and probed with secondary antibodies conjugated with horseradish peroxidase (Table S2). Once they were washed again, bands were detected through enhanced chemiluminescence using freshly prepared substrate solution based on 100 mM Tris (ThermoFisher BP152) adjusted to pH 8.5 with hydrochloric acid (ThermoFisher A144S-212), 1.2 mM luminol (Sigma A8511), 2.5 mM p-coumaric acid (Sigma C9008) and 0.04% hydrogen peroxide (w/v, Alpha Aesar L14000) on a Syngene G:BOX imager equipped with a Synoptics 4.2-megapixel camera and controlled with Syngene Genesys software.

Quantitative reverse transcription PCR

Keratinocytes were grown to confluence in 6-well tissue culture plates. For comparison between cell lines (Figure S1D), medium was switched from K-SFM to differentiation medium 24 hours before sample collection. For scratch wound experiments (Figure 2C), culture medium was switched from K-SFM to differentiation medium, then treatment samples were scratched with a 1000 mL pipette tip in a cross-hatch pattern. The scratch procedure was repeated every other day for 10 days. Samples were collected one day following the last scratch procedure. RNA was isolated from the samples using RNeasy spin column kits (Qiagen #74004) and reverse transcription was performed using SuperScript IV First-Strand Synthesis System with oligo$(dT)_{20}$ primers (Invitrogen #18091050). Real-time PCR using a C1000 thermal cycler with a CFX96 optical reaction module (Bio-Rad), iTaq Universal SYBER Green Supermix (Bio-Rad), and transcript-specific primers (Table S1) was performed to quantify transcript levels. The $2^{-\Delta\Delta C_T}$ method[12] was used to compare each individual keratin to the mean level of all keratins measured.

Keratinocyte monolayer fragmentation assay

We adopted the commonly used dispase-based fragmentation assay to verify the ability of our keratinocyte cell lines to form stable monolayer barriers[13]. Keratinocytes were seeded into collagen-coated 12-well tissue culture plates and grown to confluence. Upon reaching confluence, culture medium was changed from K-SFM to differentiation medium with additional 0.5 mM calcium chloride. After an additional 48-hour incubation, the monolayers were washed twice with PBS then incubated in dispase solution (5

units/mL in HBSS, Stemcell Technologies #07913) for 80 minutes at 37 °C to detach the monolayers from the plate. The detached monolayers were then exposed to mechanical shear stress by slow passage through a 1000µL pipette tip 10 times. Each plate was then imaged twice with an Apple iPhone 13 mini with gentle rocking between the image pairs to displace the monolayer fragments. Monolayer fragments were manually annotated and counted. If a different number of fragments was counted in each of the image pairs for a given well, the higher value was used.

Electron microscopy

Glow-discharged carbon-film gold EM grids (EMS CF200-Au) were coated with bovine type I collagen (PureCol, Advanced Biomatrix #5005) by adding one drop of a 100 µg/mL collagen solution to each grid and incubating at 37 °C for 30 minutes. The collagen solution was then removed by absorption onto a strip of filter paper. Keratinocyte cell suspensions were prepared with 10^4 cells/mL in differentiation medium, and one drop of cell suspension was added to each grid. After 24 hours, the grids were processed as follows[14]: grids were washed by dipping into 4 droplets of 'cytoskeleton buffer' (CB)[15], after wicking off the last droplet, the grids were lightly fixed and extracted in CB containing 0.25% glutaraldehyde and 0.5% Triton-X 100 for 1 minute. Grids were washed by dipping into 1 droplet of CB. The grids were then fixed for 10 minutes in CB containing 2% glutaraldehyde. After washing in 3 water droplets for 2 minutes each, the grids were stained with 1% uranyl acetate for 2 minutes; washed twice in water droplets for 2 minutes each, then air dried. Imaging was done on a JEM-1400 Plus transmission electron microscope equipped with a LaB6 source operated at 120 kV using an AMT-BioSprint 16M CCD camera. Cell junction widths were measured using ImageJ by manually drawing line regions of interest across the thickest portion of electron-dense intercellular bridges parallel to the cell-cell border.

Live imaging of monolayer migration

Sorted or mixed populations of keratinocytes were prepared depending on the experiment and seeded into collagen-coated 6-well tissue culture plates. Cells were grown to confluence, then the culture medium was changed from K-SFM to differentiation medium. After 24 hours, a linear scratch was created in each monolayer using a 1000 µL pipette tip. Monolayers were washed three times with PBS, which was then replaced with fresh differentiation medium. Samples were imaged using an inverted phase-contrast and epifluorescence Nikon ECLIPSE Ti microscope equipped with a motorized and programmable stage, a Nikon Perfect Focus System, a Hamamatsu Orca-Flash4.0 scientific CMOS camera, a SOLA solid state white-light excitation system, an OKO lab custom-built environmental chamber with temperature control and CO2 stage incubator, and Nikon Elements acquisition software. The environment was maintained at 37 °C with 5% CO_2 during the imaging period. Beginning 30 minutes after wounding, phase-contrast and fluorescence images were acquired every 6 minutes using a Plan Fluor 10× 0.3NA objective.

Analysis of migration images was based on a previously established computer vision pipeline for migration velocity estimation and wound edge detection[16]. In brief, velocity measurements were computed from the phase-contrast images using a particle image velocimetry (PIV)-based method with a 15-µm square patch size. The pipeline includes a correction for possible microscope stage drift. Monolayer contours were then determined by segmentation of the velocity map, based on the intuition that while the cells are moving, there should be no motion in the empty wound area. The algorithm imposes two additional constraints to increase robustness of the segmentation. First, the monolayer is assumed to be a continuous region. Second, the monolayer contour is assumed to move monotonically in one direction. The second condition means that the pipeline will fail if the monolayer edge retracts. Monolayers where this occurred were excluded from the analysis. While the pipeline is robust to the presence of stationary debris or irregularities in the surface of the wound area, floating debris may interfere with velocity estimation and identification of the monolayer contour. Therefore, images with floating debris were also excluded from the analysis.

Downstream analysis steps were performed using custom MATLAB scripts. For uniform cell populations, two measures of migration were calculated. First, local migration speed, as estimated by particle image velocimetry, was averaged over an area between 10-µm and 200-µm from the monolayer contour. Because the monolayer contour as estimated from 15-µm PIV patches is necessarily imprecise, the 10-µm closest to the monolayer contour was excluded. Average local migration speed followed a consistent pattern, quickly increasing to a peak speed, then gradually declining over the course of the experiment (Figures S2B and 4C). However, the timing of this peak varied between individual scratch wounds. For more robust comparisons, migration speeds traces were aligned in time based on the time of peak migration speed for each wound. Second, area closed was calculated based on advancement of the monolayer contour. This measure was not adjusted for differences in timing of peak migration speed.

For mixed cell populations, monolayers were additionally segmented into regions with different keratin expression patterns. To accomplish this, each of the fluorescence images corresponding to tagged keratins were segmented using the Rosin thresholding method[17]. These masks were then used to define high and low expression regions for each keratin. Average local migration speeds were calculated separately for each keratin expression region in the 10-µm to 200-µm band from the monolayer contour, as well as for the band as a whole. As with the analysis for uniform cell populations, migration speed traces were aligned in time based on the time of peak migration speed. Since area closed is an overall measure that does not allow comparisons between different keratin expression regions, it was not considered in analysis of the mixed population monolayers.

Fixed imaging of monolayer migration

Sorted or mixed populations of keratinocytes were prepared and seeded onto collagen-coated 18 mm-diameter #1.5 coverslips in tissue culture dishes. After cells were grown to confluence, the culture medium was switched from K-SFM to differentiation medium. After 4 hours, a line scratch was created in each coverslip using a 1000 µL pipette tip. The cultures were then returned to the incubator for 24 hours to allow migration to occur. After that period, coverslips were removed from the incubator, washed 3 times with PBS, incubated in 4% paraformaldehyde (Electron Microscopy Sciences #15713) in PBS for 10 minutes, incubated in 0.1% Triton X-100 in PBS for 8 minutes, and washed 3 more times with PBS. For experiments involving immunofluorescence labeling, samples were incubated in primary antibody diluted in PBS for 30 minutes at 37 °C (Table S2), washed 3 times with PBS, incubated in fluorophore-conjugated secondary antibody diluted in PBS for 30 minutes at 37 °C (Table S2), and washed 3 more times with PBS. Finally, coverslips were mounted onto glass slides using Fluoromount-G with DAPI (ThermoFisher 00-4959-52).

For analysis of relative enrichment of cells from a mixed population with different keratin expression levels at the monolayer edge (Figure S2E), slides were imaged using an inverted epifluorescence Nikon ECLIPSE Ti microscope equipped with a Zyla sCMOS camera (Andor), SOLA solid state white-light excitation system, and µManager acquisition software[18]. Partially overlapping images were acquired using a Plan Fluor 40× 1.3NA objective, then stitched together pairwise using the Fiji Image Stitching Plugin[19]. Analysis was performed on the composite stitched images. Monolayer edges were manually segmented using ImageJ. Individual cells were segmented using Cellpose version 1.0 with the pretrained "cyto" model[20]. A normalized sum of the tagged keratin fluorescence signals was used as input for the cytoplasm channel, and DAPI signal was used as input for the nuclear channel. Segmentations were manually reviewed, and any image areas with grossly incorrect cell segmentations were excluded from analysis. A custom Python script was used for downstream analysis. The median tagged keratin fluorescence signal was calculated for each cell. Cells were annotated as expressing high or low levels of each keratin using a linear discriminator function developed based on thresholds set between bimodal peaks in the fluorescence signal distributions. The fraction of cells expressing a high level of each keratin was then compared between the first 100-µm from the monolayer edge and the next 400-µm.

For immunofluorescence imaging of endogenous keratin expression in migrating monolayers (Figure 2A-B), slides were imaged using an inverted epifluorescence Nikon ECLIPSE Ti microscope equipped with a Zyla sCMOS camera (Andor), SOLA solid state white-light excitation system, and µManager acquisition software[18]. Images were acquired using Plan Apo 20× 0.75NA and Plan Apo 40× 1.3NA objectives. For immunofluorescence imaging of vimentin expression (Figure S6), slides were imaged using an inverted phase-contrast and epifluorescence Nikon ECLIPSE Ti microscope equipped with a motorized and programmable stage, a Nikon Perfect Focus System, a Hamamatsu Orca-Flash4.0 scientific CMOS camera, a SOLA solid state white-light excitation system, an OKO lab custom-built environmental chamber with temperature control and CO2 stage incubator, and Nikon Elements acquisition software. Images were acquired using a Plan Apo 60× 1.4NA objective.

Live imaging of single-cell migration

Keratinocytes were sparsely seeded onto collagen-coated #1.5 glass-bottom culture dishes (Cellvis D35-20-1.5-N). Cells were imaged using an inverted phase-contrast and epifluorescence Nikon ECLIPSE Ti microscope equipped with a motorized and programmable stage, a Nikon Perfect Focus System, a Hamamatsu Orca-Flash4.0 scientific CMOS camera, a SOLA solid state white-light excitation system, an OKO lab custom-built environmental chamber with temperature control and CO2 stage incubator, and Nikon Elements acquisition software. The environment was maintained at 37 °C with 5% CO_2 during the imaging period. Beginning 22-minutes, 35-minutes, or 6-hours after seeding, fluorescence images were acquired every 3 minutes for 6 to 18-hours using a Plan Fluor 10× 0.3NA objective.

Images were analyzed using the TrackMate plugin for Fiji[21]. Cells were identified using the Laplacian of Gaussian detector, and tracks were identified using the sparse linear assignment problem tracker[22]. Downstream analysis was performed using custom R scripts. Two complementary measures of migration speed were considered. First, mean velocity of a track was defined as the length of the track divided by the track duration. Second, mean squared displacement (MSD) rate was defined as the square of track displacement (linear distance from start to end positions) divided by the track duration, averaged over the set of tracks. For freely diffusing particles, MSD increases linearly with time at a rate proportional to the diffusion coefficient[23]. Since sparsely seeded cells migrating in the absence of a directional que do not fully resemble freely diffusing particles, we do not estimate a diffusion coefficient, and instead use the MSD rate as an approximation to aggregate information from multiple tracks of potentially different lengths.

Stratified epidermal migration model

We adapted an epidermal culture model from existing protocols[24,25]. While epidermal equivalent cultures lack the fibroblast-containing dermal equivalent present in skin equivalent cultures [5], their simplified design allowed us to prepare them in removable barrier molds to model epidermal migration. To prepare epidermal cultures, polycarbonate filters with 0.4μm pore size (3.14cm^2 area, Nunc #140640) were placed in larger tissue culture dishes. Two silicone inserts, each with two chambers separated by a 500μm gap (Ibidi #80209), were then pressed firmly into place on each filter using sterile forceps.

On day 0, a cell suspension of 2.5×10^5 keratinocytes in 70μL of K-SFM was added into each chamber, and additional K-SFM was added to the culture dish to reach the level of the filter. Throughout the procedure, medium in the culture dish was refreshed every two to three days, and we verified that culture medium did not leak to the top surface of the filter outside of the silicone inserts. On day 3, culture medium was aspirated from above the filter within the silicone inserts, effectively lifting the epidermal culture to an air-liquid interface. At the same time, medium in the culture dish was changed from K-SFM to differentiation medium. On day 7, an additional 0.5 mM calcium chloride was added to the differentiation medium in the culture dish.

For migration experiments, the silicone inserts were removed on day 9 by grasping the insert and filter housing with sterile forceps and gently lifting the insert while holding the filter in place. The filter was then returned to the culture dish, maintaining epidermal cultures at an air-liquid interface during the migration period. This time point, 6 days after exposure of the culture to an air-liquid interface, corresponded with development of clear basal and suprabasal keratinocyte layers and an early cornified layer, but precedes the formation of a thick cornified layer, which was more easily disrupted during removal of the silicone inserts (Figure 2D). Cultures were either imaged live during migration or fixed at the appropriate timepoint.

Fixation, staining, and imaging of epidermal cultures

Prior to fixation, medium was aspirated from the tissue culture dish and the top and bottom surfaces of the filters were washed twice with PBS, taking care not to dislodge the epidermal cultures from the top surface of the filters. The filters were then removed from the culture dishes and incubated overnight in 4% paraformaldehyde solution at 4 °C (Electron Microscopy Sciences #15713). In preparation for paraffin embedding and sectioning, the filters were cut out from their plastic housing using a #15 scalpel blade (GF Health Products 2976#15), bisected perpendicularly to the migration edge, and embedded in a 2.5% agarose gel (Lonza SeaKem LE Agarose #50000). Samples were submitted to the UT Southwestern Histo Pathology Core Facility for paraffin embedding, sectioning, and preparation of hematoxylin and eosin (H&E) stained and unstained slides.

In preparation for immunofluorescence staining, unstained paraffin-embedded tissue sections on glass slides were deparaffinized by 3 successive 5-minute incubations in xylene followed by rehydration in 3 successive 3-minute incubations in 100% ethanol and 2 successive 2-minute incubations in deionized water. For antigen retrieval, slides were placed in Tris-EDTA buffer (10 mM Tris base, 1 mM EDTA, 0.05% Tween 20, pH 9), heated to 95 °C in a microwave oven, and incubated until the buffer cooled to room temperature, approximately 45 minutes. Slides were rinsed three times in Hanks Balanced Salt Solution (HBSS) for 5 minutes each, and a PAP pen was used to circle the tissue sections. Slides were then incubated in blocking solution [5% goat serum (Abcam ab7481), 5% bovine serum albumin (Equitech-Bio BAH65-0500), and 0.5% Triton X-100 (Sigma X100) in PBS] for 1 hour. Primary antibodies (Table S2) were diluted in PBS and incubated on the tissue sections overnight at 4 °C in a humidified chamber. Following primary antibody incubation, slides were washed 3 times with HBSS for 10 minutes each. Secondary antibodies (Table S2) were diluted in PBS and incubated on the tissue sections for 60 minutes. Finally, the slides were washed 3 times with HBSS for 10 minutes each, and a small amount of Fluoromount-G with DAPI (ThermoFisher 00-4959-52) was used to affix coverslips to the slides.

H&E slides were imaged using an Olympus BX53 upright microscope with brightfield illumination, an Olympus DP21 2.01 megapixel color CCD camera, and Plan N 4× 0.1NA, 10× 0.25NA, 20× 0.4NA, and 40× 0.65NA objectives. For migration assays, the gap width between epidermal culture pairs was measured using ImageJ by manually drawing polyline regions of interest along the filter in the gap. Immunofluorescence slides were imaged using an inverted epifluorescence Nikon ECLIPSE Ti microscope equipped with a Zyla sCMOS camera (Andor), SOLA solid state white-light excitation system, and μManager acquisition software[18]. Partially overlapping images were acquired using a Plan Fluor 40× 1.3NA objective, then stitched together pairwise using the Fiji Image Stitching Plugin[19].

Live imaging of epidermal culture migration

Epidermal cultures were imaged using an inverted phase-contrast and epifluorescence Nikon ECLIPSE Ti microscope equipped with a motorized and programmable stage, a Nikon Perfect Focus System, a Hamamatsu Orca-Flash4.0 scientific CMOS camera, a SOLA solid state white-light excitation system, an OKO lab custom-built environmental chamber with temperature control and CO2 stage incubator, and Nikon Elements acquisition software. With epidermal cultures on filters sitting in tissue culture dishes placed on the stage of the inverted microscope, images were acquired from below, through the semi-translucent filter (Figure 3H). The environment was maintained at 37 °C with 5% CO_2 during the imaging period. Beginning 15 minutes after barrier removal, fluorescence images were acquired every 12 minutes using a Plan Fluor 10× 0.3NA objective.

Although resolution was limited by imaging through the filters, bright fluorescence signals from the tagged keratin constructs allowed us to identify cell locations. To analyze the resulting fluorescence images, we modified the monolayer migration analysis pipeline described above[16] as follows: First, all images were smoothed using a Gaussian filter with a 3.25-μm (5 pixel) standard deviation to decrease the influence of the filter mesh pattern on the PIV calculations. Second, since the initial texture-based segmentation seed frequently failed with fluorescence images instead of phase-contrast images, we used Otsu thresholding as an alternative[26]. Finally, because interpretation of the PIV-based local velocity estimates was complicated by potential differences in cell motion at different vertical levels within the three-dimensional epidermal culture, migration distance and speed calculations were based only on the distance travelled by the monolayer contour.

Keratin filament network segmentation and analysis

Keratinocyte cell lines expressing fluorescently tagged keratins were seeded onto collagen-coated #1.5 glass-bottom culture dishes (Cellvis D35-20-1.5-N). For knockdown experiments, cells were transduced with lentivirus to express targeting shRNA (Table S1) or a scrambled control 72 hours before analysis. Once cells grew to discrete colonies, but before reaching confluence, the culture medium was switched from K-SFM to differentiation medium. After 8 hours, cells were imaged using an inverted phase-contrast and epifluorescence Nikon ECLIPSE Ti microscope equipped with a motorized and programmable stage, a Nikon Perfect Focus System, a Hamamatsu Orca-Flash4.0 scientific CMOS camera, a SOLA solid state white-light excitation system, an OKO lab custom-built environmental chamber with temperature control and CO2 stage incubator, and

Nikon Elements acquisition software. The environment was maintained at 37 °C with 5% CO_2 during the imaging period. Images were acquired every 1 minute for 4 minutes using a Plan Apo 60× 1.4NA objective, generating an effective pixel size in object space of 108 nm. For applicable experiments, 30 μM blebbistatin (Sigma B0560), 5 μM Y27632 (Selleckchem S1049), 1 μM GSK 269962A (Selleckchem S7687), or DMSO (Fisher BP231) control were added 1 hour (blebbistatin) or 2 hours (other inhibitors) prior to imaging.

Images were analyzed using the previously published Filament Network Analysis package written in MATLAB[27]. In brief, the pipeline segments the filament network using a multi-scale steerable filter and iterative graph matching to connect fragments into complete filaments. The pipeline also calculates the local structural similarity of two filament networks based on the distance and orientation of individual filament pixels in the networks. Each pixel in the first network is matched to the closest pixel in the second network within a defined radius, and vice versa. A radius of 2.2 μm was used for all studies here. For each matched pair, the difference in position and filament orientation are calculated and used to create distance and angle maps, which are spatially smoothed by a Gaussian filter, combined, and scaled so the final similarity score decreases monotonically from 1 to 0 as the distance increases to the search radius or the angle increases to π/3. The dynamics score is defined as 1 minus the combined similarity score. The final dynamics score is 0 for identical networks and increases to 1 with increasing local differences in filament position or orientation.

To measure the effect of keratin filament composition on filament network dynamics within cells, the keratin filament images at baseline were compared to images 1, 2, 3, or 4 minutes later (Figure 5A). Because this analysis cannot reliably distinguish movement of filaments within cells from movement of the cells themselves, all image sequences were pre-screened to ensure that only stationary cells were included in the analysis. Cells were manually segmented using ImageJ, and the Filament Network Analysis Package was run to segment the keratin filament networks and calculate dynamics score maps (Figure 5B-D). The dynamics score map was then averaged over each cell area mask, excluding regions without a filament match. As a check, a quality score was computed for each cell, defined as the fraction of the cell mask area with a filament match, which was typically higher than 0.9. Image sequences of cells with low quality scores were reviewed by visual inspection. They tended to show failed filament segmentation due to low signal-to-noise ratio, debris, or cell movement, which was missed in the initial screen; these cells were excluded from subsequent analysis. For the filament dynamics analysis of keratinocytes expressing different levels of multiple keratins, the quality score on each channel also served as a robust marker of high versus low expression of each keratin, with clear bimodal distributions (Figure S3I).

In addition to the dynamics score, the Filament Network Analysis package was used to calculate additional keratin filament network properties from the baseline keratin filament segmentation. Filament density was defined as the fraction of cell area pixels segmented as filaments. Filament straightness was defined as the ratio of the linear start to end distance to the filament length. Filament curvature was defined as the mean curvature of a polynomial fit at each pixel along the filament. The median filament length, straightness, and curvature were calculated for each cell. An alternate cell summary measure of filament curvature was also calculated as the median curvature of each pixel in all filaments in the cell.

Traction force microscopy

Silicone gel substrates for traction force microscopy (TFM) were prepared in #1.0 glass-bottom 35-mm tissue culture dishes (Cellvis D35-14-1.0-N). Prepolymers for high-refractive index (n = 1.49) 8-kPa gels were prepared by mixing components A and B of QGel 920 (Quantum Silicones) in a 1:1.15 ratio as previously described[28,29]. The prepolymers were spread onto the coverglass bottoms of the dishes by spinning at 1,250 r.p.m for 30 seconds in a spin-coater (Laurell Technologies WS-650Mz-23NPPB), then cured at 100 °C for 2 hours, producing gels approximately 35-μm thick. The gels were then treated with 5% (3-aminopropyl)triethoxysilane (APTES) in ethanol to functionalize their surfaces. To allow for visualization and tracking of substrate deformation, 40-nm carboxylate far-red fluorescent beads were covalently linked to the gel surfaces by incubating the gels under a suspension of the beads (1:5,000 dilution from the 5% stock suspension) in 40-mM HEPES, pH 8, with 0.01% 1-ethyl-3-(3-dimethylaminopropyl) carbodiimide (EDC) as a catalyst. To facilitate cell adhesion during cell seeding, the substrates were coated with fibronectin by incubation with 50-μg/ml of fibronectin and 1 mg/ml EDC in PBS for 15 minutes at room temperature. The coated dishes were washed three times with PBS and filled with cell culture medium before cell seeding.

To measure keratinocyte traction force generation, 4×10^4 cells were seeded onto a substrate in differentiation medium, then returned to the incubator for 4.5 hours to allow attachment to occur. For knockdown experiments, cells were transduced with lentivirus to express targeting shRNA or a scrambled control 72 hours before seeding onto TFM substrates. Following attachment, cells were imaged using a GE DeltaVision OMX SR inverted microscope equipped with a motorized and programmable stage, three PCO sCMOS cameras, solid state lasers (405nm, 488nm, 568nm, and 640nm), and environment control. Images of the substrate beads and keratin tags were acquired in Ring-TIRF mode with a U Plan Apo 60× 1.49NA objective (generating an effective pixel size in object space of 80 nm), with imaging performed at 37 °C. Following initial imaging, during which cell positions were recorded, a prewarmed solution of dilute bleach was added to remove cells from the substrate, thereby allowing repeat imaging of the same locations with the substrate in its relaxed, strain-free state.

Image analysis was performed using the previously published TFM package written in MATLAB[29,30]. Briefly, the substrate deformation field was determined by tracking the displacement of each bead between the deformed and relaxed images using cross-correlation analysis. The displacement field, after outlier removal and stage drift correction, was then used to estimate the traction field over areas of interest surrounding each cell. Traction fields were estimated using the boundary element method [29]. While more computationally intensive than the more commonly used Fourier transform traction cytometry method, the boundary element method allows L1-norm rather than L2-norm regularization, which resolves force variation at shorter length scales[29]. A regularization parameter of 0.05 was selected based on L-curve analysis of a subset of images[29]. This parameter value was applied to all images analyzed to permit comparison of the resulting force fields. Cell area was segmented based on the tagged keratin signal. Since this signal did not always clearly extend to the cell boundary (for example, Figure 6A), masks were dilated by 1.6 μm (20 pixels), although we verified that the precise amount of dilation did not meaningfully affect the results (Figure S4C). Strain energy, which represents the mechanical work of the cell on the elastic substrate, was calculated as ½ × (displacement · traction), integrated over the segmented cell area[31].

Proximity ligation assay

Mixed populations of keratinocytes were prepared and seeded onto 8-chamber glass slides with removable wells (Lab-Tek, ThermoFisher #154534). Cells were grown to approximately 50% confluence, then culture medium was switched from K-SFM to differentiation medium for 24 hours. For knockdown experiments, cells were transduced with lentivirus to express targeting shRNA (Table S1) or a scrambled control 72 hours before processing. Slides were removed from the incubator and washed three times with PBS. For experiments using antibodies against keratins, the slides were incubated in methanol for 2 minutes. For other experiments, the slides were incubated in 4% paraformaldehyde in PBS for 10 minutes, then incubated in 0.1% Triton X-100 in PBS for 8 minutes. Slides were then washed twice with PBS and processed using Duolink Proximity Ligation Assay (PLA) reagents (In-Situ PLA Probe Anti-Mouse MINUS, Sigma DUO92004; In-Situ PLA Probe Anti-Rabbit PLUS, Sigma DUO92002; In-Situ Detection Reagents FarRed, Sigma DUO92013) according to the manufacturer's in situ fluorescence protocol. Briefly, slides were incubated in the provided Blocking Solution for 60 minutes, incubated in primary antibodies diluted in the provided Antibody Dilutant solution for 30 minutes (Table S2), incubated in PLA probe solution for 60 minutes, incubated in the ligation solution for 30 minutes, and incubated in the amplification solution for 100 minutes, with washes in the provided buffers between each step. Finally, a #1.5 cover glass was affixed to the slide using Duolink In-Situ Mounting Medium with DAPI (Sigma DUO82040).

Slides were imaged using an inverted phase-contrast and epifluorescence Nikon ECLIPSE Ti microscope equipped with a motorized and programmable stage, a Nikon Perfect Focus System, a Hamamatsu Orca-Flash4.0 scientific CMOS camera, a SOLA solid state white-light excitation system, an OKO lab custom-built environmental chamber with temperature control and CO2 stage incubator, and Nikon Elements acquisition software. Images were acquired on the tagged keratin, PLA reaction, and DAPI channels using a Plan Apo 60× 1.4NA objective (generating an effective pixel size in object space of 110 nm). Image analysis was performed using custom Python and MATLAB scripts. Individual cells were segmented using

Cellpose version 1.0 with the pretrained "cyto" model[20]. A normalized sum of the tagged keratin fluorescence signals was used as input for the cytoplasm channel, and DAPI signal was used as input for the nuclear channel. The median tagged keratin fluorescence signal was calculated for each cell. Cells were annotated as expressing high or low levels of each keratin using an empiric linear discriminator function developed based on review of the distribution of median signals. Segmentations and classifications were manually reviewed, and any incorrectly segmented or classified cells were excluded from analysis. Cells that were poorly adhered to the slide or out of focus were also excluded. Next, individual local intensity clusters in the scaled PLA image were detected using previously published MATLAB code combining wavelet denoising and multiscale products of wavelet coefficients[32,33]. Finally, PLA detections were counted within each segmented cell mask, and the density of PLA detections was compared between cells with different keratin expression levels.

Proximity biotin labeling screen

Keratinocytes were transduced with lentivirus to express K5 or K6A linked to a small promiscuous biotin ligase[8]. Because these constructs lack a selection marker, a mixed-population lentivirus was prepared by combining the tagged keratin constructs with an EGFP marker construct (see "Plasmids," above) at a molar ratio of 100:1. Cells were selected by fluorescence activated cell sorting as described above. Each cell line was then grown to confluence in collagen-coated 10 cm tissue culture plates and switched from K-SFM to differentiation medium for 24 hours before beginning the experiment.

Two independent experimental replicates were performed. Cells were incubated with 100 μM biotin for 1 hour and lysed in JS buffer (50 mM Tris HCl pH7.5, 150 mM NaCl, 5 mM EGTA, 1.5 mM $MgCl_2$, 1% Glycerol and 1% Triton X-100) supplemented with protease and phosphatase inhibitors (Halt Protease and Phosphatase Inhibitor, Thermo). Cleared lysates were incubated with Protein A Sepharose beads to remove proteins with nonspecific binding to the beads. The resulting supernatant (1 mg) was incubated with 100 μl of streptavidin-coated magnetic beads (Dynabeads MyOne Streptavidin T1 beads, Invitrogen) overnight at 4 °C with rotation to enrich for biotinylated proteins. Beads were washed three times with ice-cold JS buffer and in-gel digested for Mass Spectrometry analysis.

Proteomics data was analyzed using the DEP package for differential enrichment analysis of proteomics data in R[34]. Only proteins with no missing values in at least one of the two cell lines were included in the analysis. Abundance data was background-corrected and normalized by variance stabilizing transformation[35], and any remaining missing values were imputed as draws from a Gaussian distribution centered on quantile 0.005 of the observed values with standard deviation equal to the median standard deviation of the observed values[36]. Differential enrichment was estimated based on protein-wise linear models and empirical Bayes statistics[37], and local false discovery rates were estimated using the fdrtool package[38,39]. Functional analysis was then performed using the clusterProfiler package[40]. We searched for overrepresentation of proteins with at least 3-fold enrichment and adjusted $P < .05$ in the Gene Ontology Biological Process annotation set[41,42] using Fisher's exact test, with adjustment for multiple comparisons[43]. Because the small size of the screen limited our statistical power, we restricted our search to high-level labels with between 750 and 5,000 annotated genes.

Analysis of cell-cell junction density

Cells were prepared and seeded onto collagen-coated 18-mm-diameter #1.5 coverslips in tissue culture dishes. After reaching 25% confluence, the culture medium was switched from K-SFM to differentiation medium. After 5 hours, coverslips were removed from the incubator, washed 3 times with PBS, incubated in 4% paraformaldehyde (Electron Microscopy Sciences #15713) in PBS for 10 minutes, incubated in 0.1% Triton X-100 in PBS for 8 minutes, and washed 3 more times with PBS. Coverslips were then incubated in either Alexa Fluor 488 phalloidin (ThermoFisher A12379) or Alexa Fluor 555 phalloidin (ThermoFisher A34055) diluted 1:400 in PBS for 30 minutes at 37 °C. Finally, coverslips were mounted onto glass slides using Fluoromount-G with DAPI (ThermoFisher 00-4959-52). Slides were imaged using an inverted Nikon Ti-Eclipse microscope equipped with a pco.edge sCMOS camera with 6.5-μm pixel size (PCO), an Andor Diskovery illuminator coupled to a Yokogawa CSU-X1 confocal spinning disk head with 100 nm pinholes, and an Apo TIRF 60× 1.49NA objective (Nikon) with an additional 1.8× tube lens (yielding a final magnification of 108×; Andor Technology). This setup generated an effective pixel size in object space of 120 nm. Actin and keratin filament networks were segmented using the Filament Network Analysis package as described above in the section "Keratin filament network segmentation and analysis" based on images of phalloidin and tagged keratins respectively[27]. Approximate cell-cell boundaries were manually annotated using ImageJ. Adherens junctions and desmosomes, defined as segmented actin and keratin filaments crossing annotated cell-cell boundaries, were counted using the SlideSet plugin with a custom analysis plugin written in Java[44]. Junction density was defined as the number of junctions detected along a cell-cell boundary divided by the length of the boundary. To account for potential inconsistency in the start and end positions of the manually annotated cell-cell boundaries, boundary length was trimmed by the outermost junctions. Junction density was then compared between cell lines with different keratin expression levels.

Cell death assay

Cells were prepared and 5.5×10^4 cells were seeded onto collagen-coated 35-mm #1.5 glass-bottom culture dishes (Cellvis D35-20-1.5-N). After 4 hours of incubation, cells were transduced with lentivirus to express targeting shRNA or a scrambled control. Cells were cultured with shRNA expression for 120 hours with regular culture medium changes. H2B-mCherry3 co-expression from the shRNA constructs allowed us to confirm an infection efficiency close to 100% (see "Plasmids" above). Following the growth period, cells were incubated in SYTOX Deep Red Nucleic Acid Stain dissolved in K-SFM (0.5 μM final concentration; ThermoFisher S11381) for 30 minutes at 37 °C, then washed twice with PBS. Cells were imaged using an inverted epifluorescence Nikon ECLIPSE Ti microscope equipped with a motorized and programmable stage, a Nikon Perfect Focus System, a Hamamatsu Orca-Flash4.0 scientific CMOS camera, a SOLA solid state white-light excitation system, an OKO lab custom-built environmental chamber with temperature control and CO2 stage incubator, and Nikon Elements acquisition software. Images of the SYTOX dye, tagged keratins, and tagged H2B were acquired with a Plan Apo 60× 1.4NA objective, generating an effective pixel size in object space of 108 nm.

Individual cells were segmented using Cellpose version 1.0 with the pretrained "cyto" model[20]. First, the tagged keratin fluorescence signal was used as input for the cytoplasm channel, and no input was provided for the nuclear channel. Second, the tagged H2B signal was used as input for the "cytoplasm" channel, and no input was provided for the "nuclear" channel. This produced whole cell and nuclear masks respectively. Segmentations were manually reviewed, and any image areas with grossly incorrect cell segmentations were excluded from analysis. A custom Python script was used for downstream analysis. The median SYTOX signal within the nuclear mask was calculated for each whole cell mask. Cells were annotated as either SYTOX-negative (live) or SYTOX-positive (dead) based on comparison of the median SYTOX signal to a threshold set between bimodal peaks in the SYTOX signal distribution.

Cell proliferation assay

Cells were prepared and seeded into collagen-coated 12-well tissue culture plates, 4×10^4 cells per well. For knockdown experiments, cells were transduced with lentivirus to express targeting shRNA or a scrambled control after 4 hours, then analyzed after 96 hours with regular changes of culture medium. H2B-mCherry3 co-expression from the shRNA constructs allowed us to confirm an infection efficiency close to 100% (see "Plasmids" above). For direct cell line comparisons without shRNA knockdown, cells were analyzed after 4 days in standard culture conditions. Following the growth period, cells were incubated in 5-ethynyl-2'-deoxyuridine (EdU; ThermoFisher A10044) dissolved in K-SFM (20 mM final concentration) for 60 minutes at 37 °C. Cells were then washed 3 times with PBS, incubated in 4% paraformaldehyde (Electron Microscopy Sciences #15713) in PBS for 10 minutes, incubated in 0.1% Triton X-100 in PBS for 8 minutes, and washed 3 more times with PBS. To detect EdU incorporation into nuclear DNA, cells were incubated in a reaction mixture containing 20 mg/mL L-ascorbic acid (Sigma A92902), 0.5 mg/mL anhydrous copper(II) sulfate (Acros #42287), and 1 μM Cy5-azide (Sigma #777323) in PBS for 30 minutes at 37 °C. Cells were washed 3 times with PBS, then incubated in DAPI (ThermoFisher D1306) diluted 1:5,000 in PBS for 15 minutes at room temperature to provide a nuclear counter-stain. After 3 final washes in PBS, cells were imaged using an inverted phase-contrast and epifluorescence Nikon ECLIPSE Ti microscope equipped with a motorized and programmable stage, a Nikon Perfect Focus System, a Hamamatsu Orca-Flash4.0 scientific CMOS camera, a SOLA solid state white-light excitation

system, an OKO lab custom-built environmental chamber with temperature control and CO2 stage incubator, and Nikon Elements acquisition software. DAPI and Cy5 images were acquired using a Plan Fluor 10× 0.3NA objective, generating an effective pixel size in object space of 650 nm.

Images were segmented using Cellpose version 1.0 with the pretrained "cyto" model[20]. The DAPI signal was used as input for the "cytoplasm" channel, and no input was provided for the "nuclear" channel, producing cell nucleus masks. The median Cy5 signal was calculated for each mask, and cells were annotated as EdU-positive (Cy5-high, proliferating) or EdU-negative (Cy5-low, quiescent) based on comparison of the median Cy5 signal to a threshold set between bimodal peaks in the Cy5 signal distribution.

Imaging of clinical wound samples

Routine skin biopsies performed for diagnostic purposes result in epidermal wounds, which typically heal over 2 to 6 weeks. If a malignant lesion is identified in the biopsy, an excision may be recommended to ensure that the malignancy is completely removed. If an excision is performed before the biopsy wound has completely healed, the resulting specimen will incidentally contain the re-epithelializing biopsy wound edges. We obtained anonymized H&E stained and unstained tissue sections from an excision specimen in which the re-epithelizing biopsy wound edges were visible, but no residual carcinoma was present. Unstained slides were processed for immunofluorescence and imaged using the procedures describe above in "Fixation, staining, and imaging of epidermal cultures." This study was approved by the UT Southwestern Institutional Review Board.

Clinical sample transcriptomics analysis

Two previously published transcriptomics datasets comparing wounded to intact skin were reanalyzed for keratin expression using custom R scripts. Iglesias-Bartolome and colleagues collected serial punch biopsy specimens from the arm and buccal mucosa, extracted RNA from the samples, and performed RNA sequencing[45]. Unwounded skin was represented by the initial samples, and wounded skin was represented by follow-up samples taken from the same locations. We downloaded the expression data (Gene Expression Omnibus GSE97615) for the arm skin samples and plotted keratin transcript levels (log-transformed RPKM) as a heatmap. Statistical analysis was not performed. Ramirez and colleagues collected tissue samples from diabetic foot ulcers and non-ulcerated foot skin, extracted RNA from the samples, and profiled transcripts using Affymetrix GeneChip Human Gene 2.0 ST microarrays[46,47]. We downloaded the expression data (Gene Expression Omnibus GSE80178) and used the "oligo" R package to import, annotate, and preprocess the microarray data, including background-correction and normalization using the RMA algorithm[48]. Keratin expression intensity values for wound and control samples were plotted as a heatmap, and statistical analysis was not performed.

Statistical analysis

All statistical analysis was performed using R (R Foundation for Statistical Computing). The Kruskal-Wallis rank sum test was used to evaluate non-parametric scaled data, with Dunn's method for multiple comparisons used for experiments involving more than two groups[49]. Two-tailed *P* values less than 0.05 are considered to be significant, and are shown in figures or indicated in legends.

Typesetting

LaTeX template based on https://github.com/quantixed/manuscript-templates.

Methods References

1 Vaughan, M. B., Ramirez, R. D., Andrews, C. M., Wright, W. E. & Shay, J. W. H-ras expression in immortalized keratinocytes produces an invasive epithelium in cultured skin equivalents. *PLoS One* **4**, e7908 (2009). https://doi.org:10.1371/journal.pone.0007908

2 Ramirez, R. D. *et al.* Bypass of telomere-dependent replicative senescence (M1) upon overexpression of Cdk4 in normal human epithelial cells. *Oncogene* **22**, 433-444 (2003). https://doi.org:10.1038/sj.onc.1206046

3 Beckert, B. *et al.* Immortalized Human hTert/KER-CT Keratinocytes a Model System for Research on Desmosomal Adhesion and Pathogenesis of Pemphigus Vulgaris. *Int J Mol Sci* **20** (2019). https://doi.org:10.3390/ijms20133113

4 Rheinwald, J. G. & Green, H. Serial cultivation of strains of human epidermal keratinocytes: the formation of keratinizing colonies from single cells. *Cell* **6**, 331-343 (1975). https://doi.org:10.1016/s0092-8674(75)80001-8

5 Rasmussen, C., Thomas-Virnig, C. & Allen-Hoffmann, B. L. Classical human epidermal keratinocyte cell culture. *Methods in molecular biology* **945**, 161-175 (2013). https://doi.org:10.1007/978-1-62703-125-7_11

6 Shaner, N. C. *et al.* A bright monomeric green fluorescent protein derived from Branchiostoma lanceolatum. *Nature methods* **10**, 407-409 (2013). https://doi.org:10.1038/nmeth.2413

7 Lam, A. J. *et al.* Improving FRET dynamic range with bright green and red fluorescent proteins. *Nature methods* **9**, 1005-1012 (2012). https://doi.org:10.1038/nmeth.2171

8 Branon, T. C. *et al.* Efficient proximity labeling in living cells and organisms with TurboID. *Nat Biotechnol* **36**, 880-887 (2018). https://doi.org:10.1038/nbt.4201

9 Fischer, J. W., Busa, V. F., Shao, Y. & Leung, A. K. L. Structure-Mediated RNA Decay by UPF1 and G3BP1. *Mol Cell* **78**, 70-84 e76 (2020). https://doi.org:10.1016/j.molcel.2020.01.021

10 Bajar, B. T. *et al.* Improving brightness and photostability of green and red fluorescent proteins for live cell imaging and FRET reporting. *Sci Rep* **6**, 20889 (2016). https://doi.org:10.1038/srep20889

11 Wang, F., Zieman, A. & Coulombe, P. A. Skin Keratins. *Methods Enzymol* **568**, 303-350 (2016). https://doi.org:10.1016/bs.mie.2015.09.032

12 Wong, M. L. & Medrano, J. F. Real-time PCR for mRNA quantitation. *Biotechniques* **39**, 75-85 (2005). https://doi.org:10.2144/05391RV01

13 Ishii, K. *et al.* In vitro keratinocyte dissociation assay for evaluation of the pathogenicity of anti-desmoglein 3 IgG autoantibodies in pemphigus vulgaris. *J Invest Dermatol* **124**, 939-946 (2005). https://doi.org:10.1111/j.0022-202X.2005.23714.x

14 Vinzenz, M. *et al.* Actin branching in the initiation and maintenance of lamellipodia. *J Cell Sci* **125**, 2775-2785 (2012). https://doi.org:10.1242/jcs.107623

15 Mueller, J. *et al.* Load Adaptation of Lamellipodial Actin Networks. *Cell* **171**, 188-200 e116 (2017). https://doi.org:10.1016/j.cell.2017.07.051

16 Zaritsky, A. *et al.* Diverse roles of guanine nucleotide exchange factors in regulating collective cell migration. *J Cell Biol* **216**, 1543-1556 (2017). https://doi.org:10.1083/jcb.201609095

17 Rosin, P. L. Unimodal thresholding. *Pattern Recognition* **34**, 2083-2096 (2001). https://doi.org:10.1016/s0031-3203(00)00136-9

18 Edelstein, A., Amodaj, N., Hoover, K., Vale, R. & Stuurman, N. Computer control of microscopes using microManager. *Curr Protoc Mol Biol* **Chapter 14**, Unit14 20 (2010). https://doi.org:10.1002/0471142727.mb1420s92

19 Preibisch, S., Saalfeld, S. & Tomancak, P. Globally optimal stitching of tiled 3D microscopic image acquisitions. *Bioinformatics* **25**, 1463-1465 (2009). https://doi.org:10.1093/bioinformatics/btp184

20 Stringer, C., Wang, T., Michaelos, M. & Pachitariu, M. Cellpose: a generalist algorithm for cellular segmentation. *Nature methods* **18**, 100-106 (2021). https://doi.org:10.1038/s41592-020-01018-x

21 Tinevez, J. Y. *et al.* TrackMate: An open and extensible platform for single-particle tracking. *Methods* **115**, 80-90 (2017). https://doi.org:10.1016/j.ymeth.2016.09.016

22 Jaqaman, K. *et al.* Robust single-particle tracking in live-cell time-lapse sequences. *Nature methods* **5**, 695-702 (2008). https://doi.org:10.1038/nmeth.1237

23 Michalet, X. Mean square displacement analysis of single-particle trajectories with localization error: Brownian motion in an isotropic medium. *Phys Rev E Stat Nonlin Soft Matter Phys* **82**, 041914 (2010). https://doi.org:10.1103/PhysRevE.82.041914

24 Smits, J. P. H. *et al.* Immortalized N/TERT keratinocytes as an alternative cell source in 3D human epidermal models. *Sci Rep* **7**, 11838 (2017). https://doi.org:10.1038/s41598-017-12041-y

25 Rikken, G., Niehues, H. & van den Bogaard, E. H. Organotypic 3D Skin Models: Human Epidermal Equivalent Cultures from Primary Keratinocytes and Immortalized Keratinocyte Cell Lines. *Methods in molecular biology* **2154**, 45-61 (2020). https://doi.org:10.1007/978-1-0716-0648-3_5

26 Otsu, N. A Threshold Selection Method from Gray-Level Histograms. *IEEE Transactions on Systems, Man, and Cybernetics* **9**, 62-66 (1979). https://doi.org:10.1109/tsmc.1979.4310076

27 Gan, Z. *et al.* Vimentin Intermediate Filaments Template Microtubule Networks to Enhance Persistence in Cell Polarity and Directed Migration. *Cell Syst* **3**, 252-263 e258 (2016). https://doi.org:10.1016/j.cels.2016.08.007

28 Gutierrez, E. *et al.* High refractive index silicone gels for simultaneous total internal reflection fluorescence and traction force microscopy of adherent cells. *PLoS One* **6**, e23807 (2011). https://doi.org:10.1371/journal.pone.0023807

29 Han, S. J., Oak, Y., Groisman, A. & Danuser, G. Traction microscopy to identify force modulation in subresolution adhesions. *Nature methods* **12**, 653-656 (2015). https://doi.org:10.1038/nmeth.3430

30 Han, S. J. *et al.* Pre-complexation of talin and vinculin without tension is required for efficient nascent adhesion maturation. *Elife* **10** (2021). https://doi.org:10.7554/eLife.66151

31 Butler, J. P., Tolic-Norrelykke, I. M., Fabry, B. & Fredberg, J. J. Traction fields, moments, and strain energy that cells exert on their surroundings. *Am J Physiol Cell Physiol* **282**, C595-605 (2002). https://doi.org:10.1152/ajpcell.00270.2001

32 Olivo-Marin, J.-C. Extraction of spots in biological images using multiscale products. *Pattern Recognition* **35**, 1989-1996 (2002). https://doi.org:10.1016/s0031-3203(01)00127-3

33 Aguet, F., Antonescu, C. N., Mettlen, M., Schmid, S. L. & Danuser, G. Advances in analysis of low signal-to-noise images link dynamin and AP2 to the functions of an endocytic checkpoint. *Dev Cell* **26**, 279-291 (2013). https://doi.org:10.1016/j.devcel.2013.06.019

34 Zhang, X. *et al.* Proteome-wide identification of ubiquitin interactions using UbIA-MS. *Nat Protoc* **13**, 530-550 (2018). https://doi.org:10.1038/nprot.2017.147

35 Huber, W., von Heydebreck, A., Sultmann, H., Poustka, A. & Vingron, M. Variance stabilization applied to microarray data calibration and to the

quantification of differential expression. *Bioinformatics* **18 Suppl 1**, S96-104 (2002). https://doi.org:10.1093/bioinformatics/18.suppl_1.s96
36 Gatto, L. & Lilley, K. S. MSnbase-an R/Bioconductor package for isobaric tagged mass spectrometry data visualization, processing and quantitation. *Bioinformatics* **28**, 288-289 (2012). https://doi.org:10.1093/bioinformatics/btr645
37 Ritchie, M. E. *et al.* limma powers differential expression analyses for RNA-sequencing and microarray studies. *Nucleic Acids Res* **43**, e47 (2015). https://doi.org:10.1093/nar/gkv007
38 Strimmer, K. A unified approach to false discovery rate estimation. *BMC bioinformatics* **9**, 303 (2008). https://doi.org:10.1186/1471-2105-9-303
39 Strimmer, K. fdrtool: a versatile R package for estimating local and tail area-based false discovery rates. *Bioinformatics* **24**, 1461-1462 (2008). https://doi.org:10.1093/bioinformatics/btn209
40 Yu, G., Wang, L. G., Han, Y. & He, Q. Y. clusterProfiler: an R package for comparing biological themes among gene clusters. *OMICS* **16**, 284-287 (2012). https://doi.org:10.1089/omi.2011.0118
41 Ashburner, M. *et al.* Gene ontology: tool for the unification of biology. The Gene Ontology Consortium. *Nat Genet* **25**, 25-29 (2000). https://doi.org:10.1038/75556
42 Gene Ontology, C. The Gene Ontology resource: enriching a GOld mine. *Nucleic Acids Res* **49**, D325-D334 (2021). https://doi.org:10.1093/nar/gkaa1113
43 Benjamini, Y. & Hochberg, Y. Controlling the False Discovery Rate: A Practical and Powerful Approach to Multiple Testing. *Journal of the Royal Statistical Society: Series B (Methodological)* **57**, 289-300 (1995). https://doi.org:10.1111/j.2517-6161.1995.tb02031.x
44 Nanes, B. A. Slide Set: Reproducible image analysis and batch processing with ImageJ. *Biotechniques* **59**, 269-278 (2015). https://doi.org:10.2144/000114351
45 Iglesias-Bartolome, R. *et al.* Transcriptional signature primes human oral mucosa for rapid wound healing. *Sci Transl Med* **10** (2018). https://doi.org:10.1126/scitranslmed.aap8798
46 Ramirez, H. A. *et al.* Staphylococcus aureus Triggers Induction of miR-15B-5P to Diminish DNA Repair and Deregulate Inflammatory Response in Diabetic Foot Ulcers. *J Invest Dermatol* **138**, 1187-1196 (2018). https://doi.org:10.1016/j.jid.2017.11.038
47 Ramirez, H. A. *et al.* Comparative Genomic, MicroRNA, and Tissue Analyses Reveal Subtle Differences between Non-Diabetic and Diabetic Foot Skin. *PLoS One* **10**, e0137133 (2015). https://doi.org:10.1371/journal.pone.0137133
48 Carvalho, B. S. & Irizarry, R. A. A framework for oligonucleotide microarray preprocessing. *Bioinformatics* **26**, 2363-2367 (2010). https://doi.org:10.1093/bioinformatics/btq431
49 Dunn, O. J. Multiple Comparisons Using Rank Sums. *Technometrics* **6**, 241-252 (1964). https://doi.org:10.1080/00401706.1964.10490181

Supplementary Figures and Tables

Table S1. Primers and synthetic DNA sequences

Primer	Sequence
pLVX-KRT5-mNG-IRES-Puro	
KRT5-F	GATCTATTTCCGGTGAATTCCTCGAGGCCACCATGTCTCGCCAGTCAAGTGTG
KRT5-R	GTACAAGAAAGCTGGGTCGCTCTTGAAGCTCTTCCGGGAG
mNG-F	GACCCAGCTTTCTTGTACGTGAGCAAGGGCGAGGAG
mNG-R	GAGAGGGGCGGGATCCTTACTTGTACAGCTCGTCCATGCC
pLVX-KRT6A-mRb-IRES-Neo	
KRT6A-F	CTATTTCCGGTGAATTCCTCGAGGCCACCATGGCCAGCACATCCACC
KRT6A-R	TAGACACGTACAAGAAAGCTGGGTCTAGTGCTTATAGCTCTTCCTGCTGG
mRb-F	CACTAGACCCAGCTTTCTTGTACGTGTCTAAGGGCGAAGAGCTG
mRb-R	GAGAGGGGCGGGATCCTTACTTGTACAGCTCGTCCATCCC
Keratin chimeras	
KRT5H-F	CCGACTCTACTAGAGGATCTATTTCCGGTACTAGTGCCACCATGTCTCGCCAGTCAAGTG
KRT5H-KRT6AR-R	GTTGTTGAGGGTCTTGATCTGTTCACGCTCCTCGGTCCTCACCCTCTGGATGCTG
KRT6AR-KRT5H-F	CAGCATCCAGAGGGTGAGGACCGAGGAGCGTGAACAGATCAAGACCCTCAACAAC
KRT6AR-KRT5T-R	CTCCTTCTCCACTGAGTCTGCATTCCTCACCCTCCAGCAGCTTGCGGTA
KRT5T-KRT6AR-F	CCTACCGCAAGCTGCTGGAGGGTGAGGAATGCAGACTCAGTGGAGAAGGAGTTGG
KRT5T-mNG-R	GGGGGAGGGAGAGGGGCGGGATCCACGCGTTTACTTGTACAGCTCGTCCATGCCCATCAC
KRT6AH-F	TACTAGAGGATCTATTTCCGGTACTAGTGCCACCATGGCCAGCACATCCACCACCATCAG
KRT6AH-KRT5R-R	GAGGGTCTTGATCTGCTCGCGCTCCTCGGCCCGCACCCGCTGG
KRT5R-KRT6AH-F	CCACCATCCAGCGGGTGCGGGCCGAGGAGCGCGAGCAGATCAAGACCCTCAA
KRT5R-KRT6AT-R	AACGCCTTCGCCATTCAGCCTGCACTCCTCGCCCTCCAGCAGCTTGCGG
KRT6AT-KRT5R-F	TTACCGCAAGCTGCTGGAGGGCGAGGAGTGCAGGCTGAATGGCGAAGGC
KRT6AT-mRb-R	GGGGGAGGGAGAGGGGCGGGATCCACGCGTTTACTTGTACAGCTCGTCCATCCCACCAC
Biotin ligase constructs	
XbaI-miniTurbo-Flag-BamHI	TCTAGAATCCCGCTGCTGAACGCTAAACAGATTCTGGGACAGCTGGACGGCGGGAGCGTGGCAGTCCTGCCT GTGGTCGACTCCACCAATCAGTACCTGCTGGATCGAATCGGCGAGCTGAAGAGTGGGGATGCTTGCATTGCA GAATATCAGCAGGCAGGGAGAGGAAGCAGAGGGAGGAAATGGTTCTCTCCTTTTGGAGCTAACCTGTACCTG AGTATGTTTTGGCGCCTGAAGCGGGGACCAGCAGCAATCGGCCTGGGCCCGGTCATCGGAATTGTCATGGCA GAAGCGCTGCGAAAGCTGGGAGCAGACAAGGTGCGAGTCAAATGGCCCAATGACCTGTATCTGCAGGATAGA AAGCTGGCAGGCATCCTGGTGGAGCTGGCCGGAATAACAGGCGATGCTGCACAGATCGTCATTGGCGCCGG GATTAACGTGGCTATGAGGCGCGTGGAGGAAAGCGTGGTCAATCAGGGCTGGATCACACTGCAGGAAGCAG GGATTAACCTGGACAGGAATACTCTGGCCGCTATGCTGATCCGAGAGCTGCGGGCAGCCCTGGAACTGTTCG AGCAGGAAGGCCTGGCTCCATATCTGTCACGGTGGGAGAAGCTGGATAACTTCATCAATAGACCCGTGAAGC TGATCATTGGGGACAAAGAGATTTTCGGGATTAGCCGGGGGATTGATAAACAGGGAGCCCTGCTGCTGGAAC AGGACGGAGTTATCAAACCCTGGATGGGCGGAGAAATCAGTCTGCGGTCTGCCGAAAAGGATTACAAGGACG ACGATGACAAGTAAGGATCC
KRT5/6-F	CTAGAGGATCTATTTCCGGTGAATTCCTCGAG
KRT5-R	GTTCTCTAGAGAAAGCTGGGTCGCTCTTG
KRT6A-R	GTTCTCTAGAGAAAGCTGGGTCGTGCTTATAG
pLKO.1-H2B-mRb	
H2B-mRuby3	CCGACCTCTCTCCCCAGGGGGATCCACCGGAGCTTACCATGCCAGAGCCAGCGAAGTCTGCTCCCGCCCCG AAAAAGGGCTCCAAGAAGGCGGTGACTAAGGCGCAGAAGAAAGGCGGCAAGAAGCACAAGCGCAGCCGCAA GGAGAGCTATTCCATCTATGTGTACAAGGTTCTGAAGCAGGTCCACCCTGACACCGGCATTTCGTCCAAGGCC ATGGGCATCATGAATTCGTTTGTGAACGACATTTTCGAGCGCATCGCAGGTGAGGCTTCCCGCCTGGCGCATT ACAACAAGCGCTCGACCATCACCTCCAGGGAGATCCAGACGGCCGTGCGCCTGCTGCTGCCTGGGGAGTTG GCCAAGCACGCCGTGTCCGAGGGTACTAAGGCCATCACCAAGTACACCAGCGCTAAGTCCGGTCTTCGGAGC GGCAGCGGTGGGGGCTCTGCATCAGGCGGCTCAGGGAGTATGGTGTCTAAGGGCGAAGAGCTGATCAAGGA AAATATGCGTATGAAGGTGGTCATGGAAGGTTCGGTCAACGGCCACCAATTCAAATGCACAGGTGAAGGAGA AGGCAGACCGTACGAGGGAACTCAAACCATGAGGATCAAAGTCATCGAGGGAGGACCCCTGCCATTTGCCTT TGACATTCTTGCCACGTCGTTCATGTATGGCAGCCGTACTTTTATCAAGTACCCGGCCGACATCCCTGATTTCT TTAAACAGTCCTTTCCTGAGGGTTTTACTTGGGAAAGAGTTACGAGATACGAAGATGGTGGAGTCGTCACCGT CACGCAGGACACCAGCCTTGAGGATGGCGAGCTCGTCTACAACGTCAAGGTCAGAGGGGTAAACTTTCCCTC CAATGGTCCCGTGATGCAGAAGAAGACCAAGGGTTGGGAGCCTAATACAGAGATGATGTATCCAGCAGATGG TGGTCTGAGAGGATACACTGACATCGCACTGAAAGTTGATGGTGGTGGCCATCTGCACTGCAACTTCGTGACA ACTTACAGGTCAAAAAAGACCGTCGGGAACATCAAGATGCCCGGTGTCCATGCCGTTGATCACCGCCTGGAA AGGATCGAGGAGAGTGACAATGAAACCTACGTAGTGCAACGCGAAGTGGCAGTTGCCAAATACAGCAACCTT GGTGGTGGCATGGACGAGCTGTACAAGTAAGGTACCTTTAAGACCAATGACTTACAAGGC
shVim#1-F	CCGGCTCTGGTTGATACCCACTCAACTCGAGTTGAGTGGGTATCAACCAGAGTTTTTG
shVim#1-R	GAGACCAACTATGGGTGAGTTGAGCTCAACTCACCCATAGTTGGTCTCAAAAACTTAA
shVim#2-F	CCGGGCTAACTACCAAGACACTATTCTCGAGAATAGTGTCTTGGTAGTTAGCTTTTTG
shVim#2-R	CGATTGATGGTTCTGTGATAAGAGCTCTTATCACAGAACCATCAATCGAAAAACTTAA
qRT-PCR Primers	
KRT1-F	GATTGCCACCTACAGGACCC
KRT1-R	ACAGACACACTCACGTTCGG
KRT5-F	GGAATGCAGACTCAGTGGAGA
KRT5-R	CCACTGCCATATCCAGAGGAAA

Primer	Sequence
K5-mNG-F	AAGAGCTTCAAGAGCGACCC
K5-mNG-R	AACTCATGTGTCGCTGGGAG
KRT6A-F	TTGCAGAAAATTGCCAGGGG
KRT6A-R	GGTGGGGGTTCACAACACTT
K6A-mRb-F	CCATCAAGTACACCACCACCT
K6A-mRb-R	TTGACCGAACCTTCCATGACC
KRT6B-F	GCTGGGATGCCCTCACTTTT
KRT6B-R	TTCGCATGTCTGAGTGCTGA
KRT6C-F	CGTCTCCTCAGGTTGCCTATC
KRT6C-R	CAGATGGGGCAGGTATAGACAG
KRT10-F	TTCTAGCAGCAAAGGCTCCC
KRT10-R	CAGAGCTCCCACGGCTAAAA
KRT14-F	CCAGTTCTCCTCTGGATCGC
KRT14-R	CGTGCACATCCATGACCTTG
KRT16-F	CTCTTCGAGCCGTCAGACC
KRT16-R	GTGGTAGAGGCAGCTCAGTTC
KRT17-F	GAGCAGCAGAACCAGGAATACA
KRT17-R	GGTACGCACCTGACGGG

Table S2. Antibodies

Antibody	Application and dilution
Mouse anti-keratin 1 (Novus LHK1)	WB, 1:250
Rabbit anti-keratin 5 (Abcam ab52635), N-terminal epitope	IF/PLA, 1:200
	WB, 1:10,000
	IHC, 1:200
Rabbit anti-keratin 5 (Cell Signaling Technology #25807), C-terminal epitope	WB, 1:1,000
Rabbit anti-keratin 6 (Abcam ab93279), epitope conserved in K6A, K6B, and K6C	IF, 1:50
	WB, 1:2,000
	IHC, 1:50
Rabbit anti-keratin 10 (Abcam ab76318)	WB, 1:1,000
Mouse anti-keratin 14 (EMD Millipore MAB3232)	WB, 1:200
Mouse anti-keratin 16 (Invitrogen LL025)	WB, 1:500
Rabbit polyclonal anti-keratin 17 (Abcam ab53707)	IF/PLA, 1:1,000
	WB, 1:1,000
	IHC, 1:100
Mouse anti-beta-actin (Sigma A1978)	WB, 1:5,000
Rabbit polyclonal anti-non-muscle myosin heavy chain IIA (MYH9; Invitrogen PA5-17025)	PLA, 1:200
Mouse anti-phospho-myosin regulatory light chain (Cell Signaling Technology #3675)	PLA, 1:100
Mouse anti-vimentin (Sigma V6630)	IF/PLA, 1:100
Rabbit anti-vimentin (Cell Signaling Technology #5741)	WB, 1:1,000
Rabbit anti-ROCK2 and ROCK1 (Abcam ab45171)	PLA, 1:250
Rabbit polyclonal anti-myosin light chain kinase (Invitrogen PA5-76982)	PLA, 1:200
HRP, goat anti- mouse IgG (Invitrogan #31430)	WB, 1:1,000
HRP, goat anti- rabbit IgG (Invitrogan #31460)	WB, 1:1,000
Alexa Fluor 488, goat anti- mouse IgG (Invitrogen A-11209)	IF, 1:500
Alexa Fluor 488, goat anti- rabbit IgG (Invitrogen A-11008)	IF, 1:500
Alexa Fluor 568, goat anti- mouse IgG (Invitrogen A-11004)	IF, 1:500
Alexa Fluor 568, goat anti- rabbit IgG (Invitrogen A-11036)	IF, 1:500
Alexa Fluor 647, goat anti- rabbit IgG (Invitrogen A-21244)	IF, 1:500

IF, immunofluorescence; IHC, immunohistochemistry or immunofluorescence on formalin-fixed paraffin-embedded samples; PLA, proximity ligation assay; WB, western blot

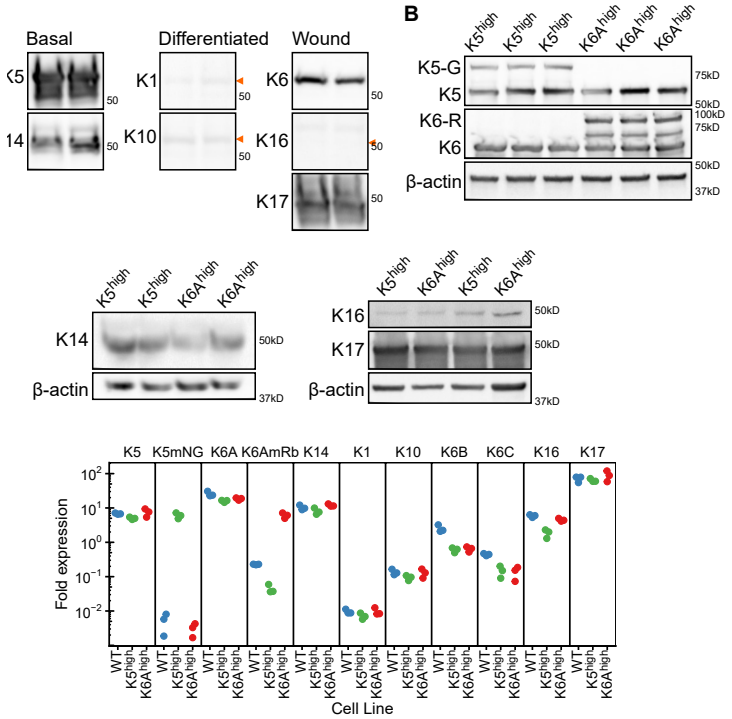

Figure S1. Keratin expression in keratinocyte culture models.

A. Western blot analysis of keratin expression in human keratinocytes grown in submerged culture. Orange arrowheads indicate expected size for protein bands not clearly visualized. Samples from two independent cultures are shown.

B. Western blot analysis of endogenous (K5, K6) and exogenously expressed (K5-G, K6-R) keratins in K5^{high} and K6A^{high} cell lines (see also Figure 3B).

C. Western blot analysis of other endogenously expressed keratins in K5^{high} and K6A^{high} keratinocyte cell lines.

D. Keratin transcript levels in parental (wt), K5^{high}, and K6A^{high} keratinocyte cell lines measured by qRT-PCR. Individual keratin transcript levels were compared to the average level of all keratin transcripts measured. *n* = 3 samples per group.

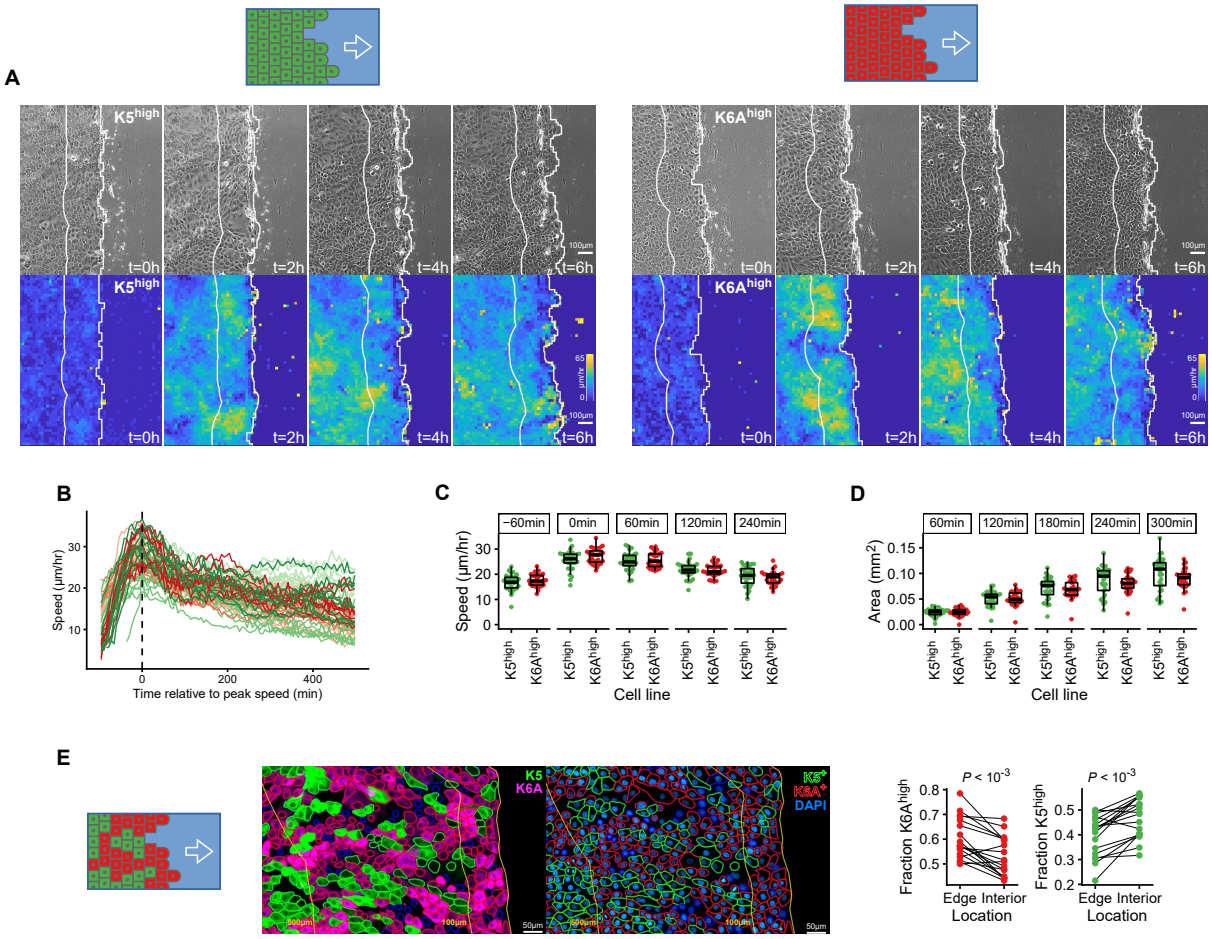

Figure S2. Wound-associated K6A supports keratinocyte migration in monolayers.

A. Uniform-population monolayers of K5^{high} or K6A^{high} cells were scratched with a pipette tip to create a wound and imaged live as cells migrated into the wound area. The migration front was tracked using a computer vision pipeline and local and global migration speeds were calculated (see Methods). Top, phase-contrast images. Bottom, local migration speed maps. White lines, 200-µm wide band tracking the wound edge. See also Video 2.

B. Time courses of average local migration speed in the area 10-µm to 200-µm from the wound edge for individual scratch wounds were aligned by the time of peak migration speed. Green, K5^{high} cells; red, K6A^{high} cells. n = 28-30 scratch wounds per group.

C-D. Comparison of average local migration speed (C) and area closed (D) for migrating K5^{high} and K6A^{high} monolayers over time. In (C), time windows are aligned relative to the time of overall peak migration speed for each monolayer. n = 28-30 scratch wounds per group.

E. Mixed population monolayers containing both K5^{high} and K6A^{high} cells were scratched to create a wound, then fixed and imaged after 24-hours of migration. Cells were segmented and classified using a computer vision pipeline (center; see Methods), then the proportion of K5^{high} and K6A^{high} cells in the 100-µm band closest to the wound edge was compared to the next 400-µm. n = 18 scratch wounds.

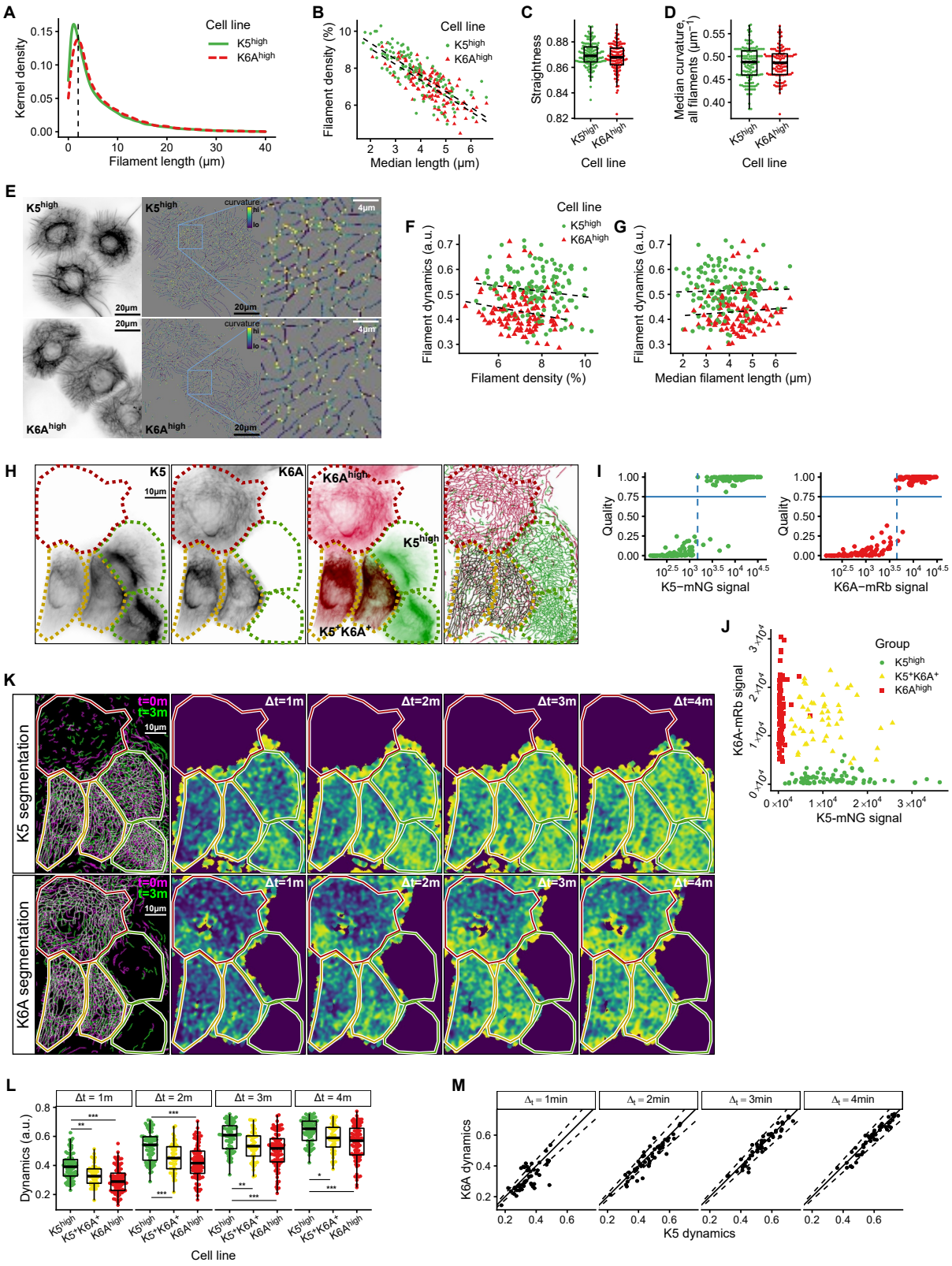
A
Kernel density
Filament length (μm)
Cell line
K5high
K6Ahhigh
B
Filament density (%)
Median length (μm)
Cell line
K5high
K6Ahhigh
C
Straightness
Cell line
D
Median curvature, all filaments (μm−1)
Cell line
E
K5high
K6Ahhigh
curvature
hi
lo
20μm
4μm
F
Filament dynamics (a.u.)
Filament density (%)
Cell line
K5high
K6Ahhigh
G
Filament dynamics (a.u.)
Median filament length (μm)
H
K5
K6A
K6Ahigh
K5high
K5+K6A+
10μm
I
Quality
K5−mNG signal
K6A−mRb signal
J
K6A-mRb signal
K5-mNG signal
Group
K5high
K5+K6A+
K6Ahigh
K
K5 segmentation
K6A segmentation
t=0m
t=3m
10μm
Δt=1m
Δt=2m
Δt=3m
Δt=4m
L
Δt = 1m
Δt = 2m
Δt = 3m
Δt = 4m
Dynamics (a.u.)
K5high
K5+K6A+
K6Ahigh
Cell line
M
Δt = 1min
Δt = 2min
Δt = 3min
Δt = 4min
K6A dynamics
K5 dynamics

Previous page: **Figure S3. Wound-associated K6A alters filament network dynamics, but not static architecture.**

A-G. Images of keratin filament networks in K5^{high} and K6A^{high} cells were segmented and the segmented as in Figure 5A-E. n = 110-139 cells per group with 1.7×10^4-2.6×10^4 total filaments per group. A, Distribution of individual segmented filament lengths in K5^{high} and K6A^{high} cells. B, Correlation between filament density, defined as the percentage of cell area pixels included in the segmented filament network, and median filament length per cell. Dotted lines, linear regression models (K5^{high}, R^2_{adj} = .61; K6A^{high}, R^2_{adj} = .56). C, Median filament straightness per cell, defined as the ratio between the end-to-end distance and length of a filament. D, Median filament network curvature, defined as the median of point curvature estimates at each pixel included in the segmented filament network. This metric limits the influence of short filaments on the summary statistic. E, Example images of filament point curvature estimates. F, Correlation between filament network dynamics (3-minute time interval) and filament density. Dotted lines, linear regression models (K5^{high}, R^2_{adj} = .01; K6A^{high}, R^2_{adj} = .03). G, Correlation between filament network dynamics (3-minute time interval) and median filament length. Dotted lines, linear regression models (K5^{high}, R^2_{adj} = <0.01; K6A^{high}, R^2_{adj} = <0.01).

H-M. Analysis of keratin filament network dynamics in a mixed culture of K5^{high}, K6A^{high}, and K5^{high}/K6A^{high} (K5$^+$K6A$^+$) cells. n = 49-87 cells per group in 68 total movies. H, Two-channel fluorescence imaging of tagged K5 and K6A in the mixed cell population. The filament networks were separately segmented on each channel (right). Dotted outlines indicate cell classification: green, K5^{high}; red, K6A^{high}; yellow, K5^{high}/K6A^{high} (K5$^+$K6A$^+$). I, Method for cellular keratin level determination. For each channel, cell filament segmentation quality scores, defined as the fraction of cell area with a dynamics score match at a 1-minute interval (see Methods), compared to the median fluorescence signal. A high score is synonymous with high fluorescent tag expression. A quality score of 0.75 (solid horizontal lines) was used to separate high from low expression levels of the keratin associated with each channel. The quality score showed better separation power than cut-offs defined by median fluorescence signal (dashed vertical lines). J, Median K5 and K6A fluorescence signals in cells classified as K5^{high}, K6A^{high}, and K5^{high}/K6A^{high} (K5$^+$K6A$^+$) based on the segmentation quality score. K, Filament segmentation and network dynamics score maps for K5^{high}, K6A^{high}, and K5^{high}/K6A^{high} cells. Outlines indicate keratin expression levels as in (H). L, Comparison of network dynamics scores between cell types. *, P < .05; **, P < .01; ***, P < 10^{-3}. M, Correlation between network dynamics scores calculated separately for the K5 and K6A channels in K5^{high}/K6A^{high} cells. The solid diagonal line indicates equal scores, the expected result for evenly intermixed keratins in a single network with perfect segmentation. Dashed lines indicate ±10% deviation. n = 49 cells in 28 movies.

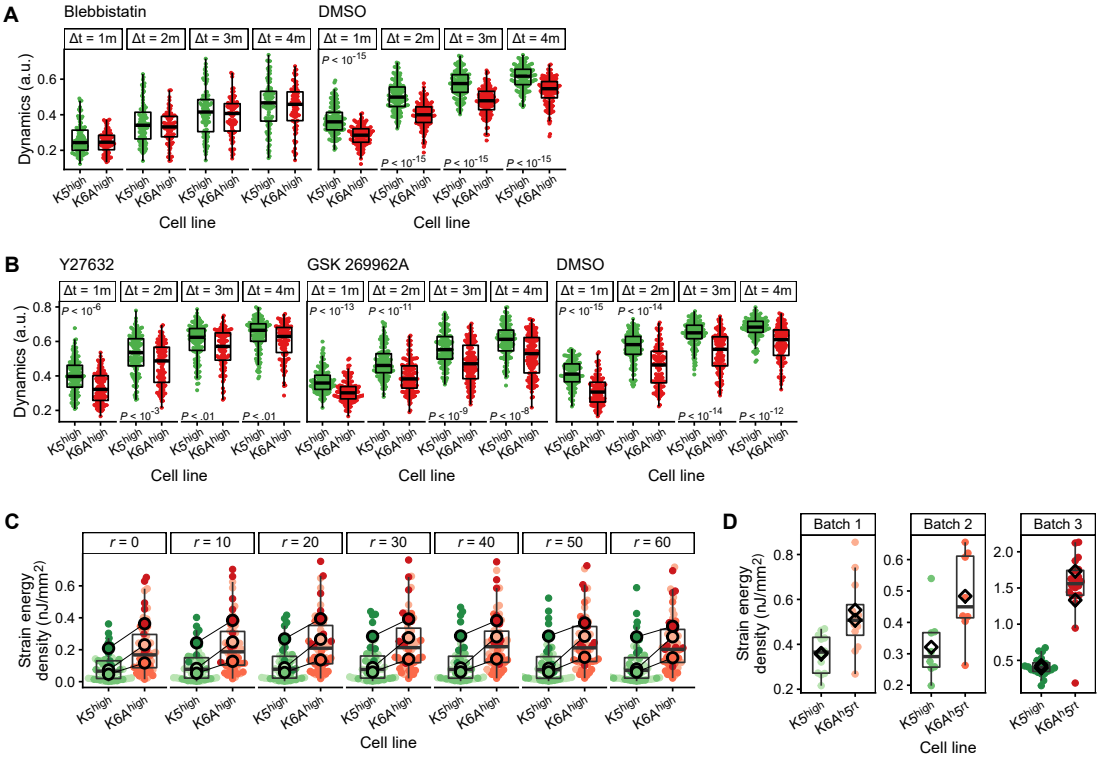

Figure S4. Network dynamics under reduced myosin motor activity and sensitivity analysis of traction force microscopy experiments.

A-B. Keratinocytes were treated with 30 μM of the myosin ATPase-inhibitor Blebbistatin or DMSO control for 1 hour (A), or with 5 μM or 1 μM of the ROCK inhibitors Y27632 and GSK 269962A respectively, or DMSO control, for 2 hours (B). After drug incubation, keratin network dynamics were measured and compared between cell lines. A, n = 81-143 cells in 27-45 movies per group. B, n = 110-144 cells in 18-20 movies per group.

C. Strain energy density of K5^{high} and K6A^{high} cells measured using traction force microscopy with different expansion radii of the cell area mask beyond visible tagged-keratin fluorescence signals. Expansion radius in pixels. See also Figure 6A. n = 51-58 cells per group.

D. Strain energy density of cells expressing a chimeric keratin containing the head domain of K6A joined to the rod and tail of K5 (K6A^{h}5^{rt}) or full-length K5, with results separated by TFM substrate batches. Diamonds indicate mean strain energy density for cells on individual TFM substates (1-2 per group per batch). See also Figure 6B. n = 40 cells per group.

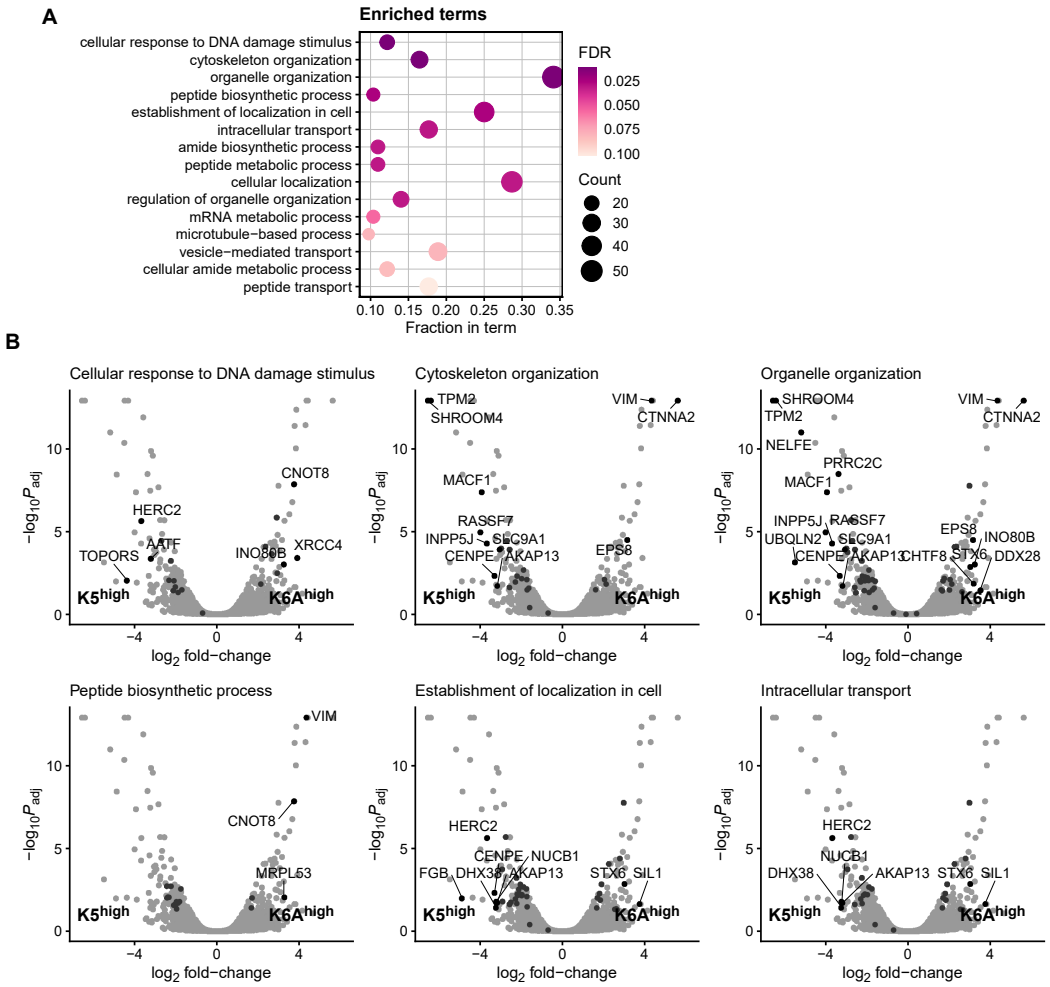

Figure S5. Proteins differentially associated with specific keratins are implicated in a variety of biological functions.

A. Most enriched Gene Ontology Biologic Process labels among proteins differentially associated with keratin filaments between K5^{high} and K6A^{high} cells, defined as greater than 3-fold differential association and P_{adj} < .05. See also Figure 7A.

B. Volcano plots highlighting differentially expressed proteins within the most enriched Gene Ontology Biologic Process labels.

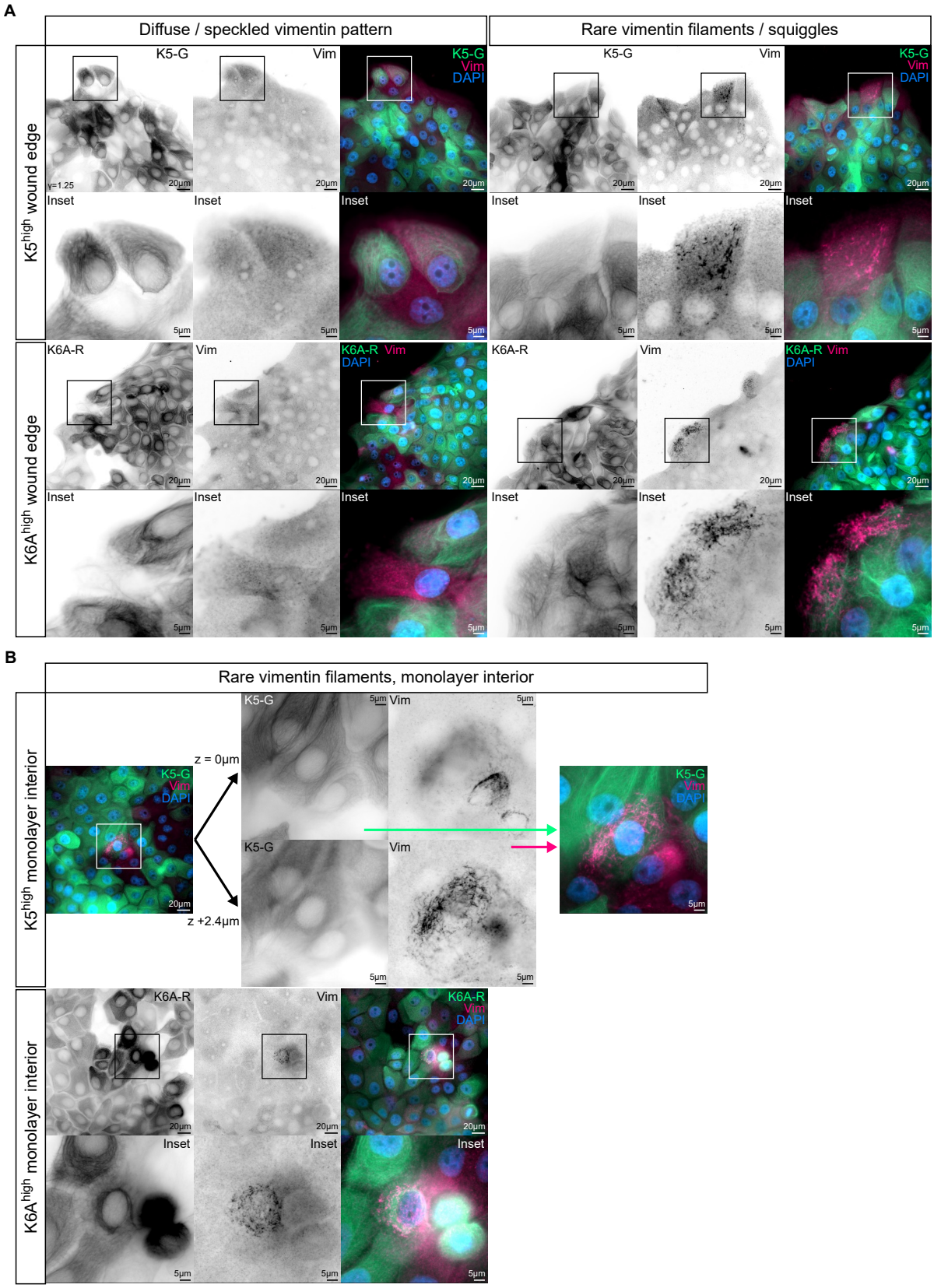

Figure S6. Non-filamentous vimentin is present throughout keratinocyte monolayers.

A. Immunofluorescence imaging of vimentin (Vim) in monolayers of K5^{high} and K6A^{high} cells. Keratins are detected by their associated fluorescent tags (K5-G, K5-mNeonGreen; K6A-R, K6A-mRuby2). Cell monolayers were scratched to create a wound area 24-hours prior to fixation and processing for imaging. Diffuse or speckled vimentin staining patterns (left columns) were typical. Cells displaying vimentin squiggles or filaments were extremely rare (right columns, not quantified).

B. Additional images highlighting rare cells away from the scratch wound edge with detectable vimentin squiggles or filaments. Top row center insets compare keratin and vimentin images in different focal planes. Top row right inset overlays keratin and vimentin images from different focal planes with the sharpest focus.

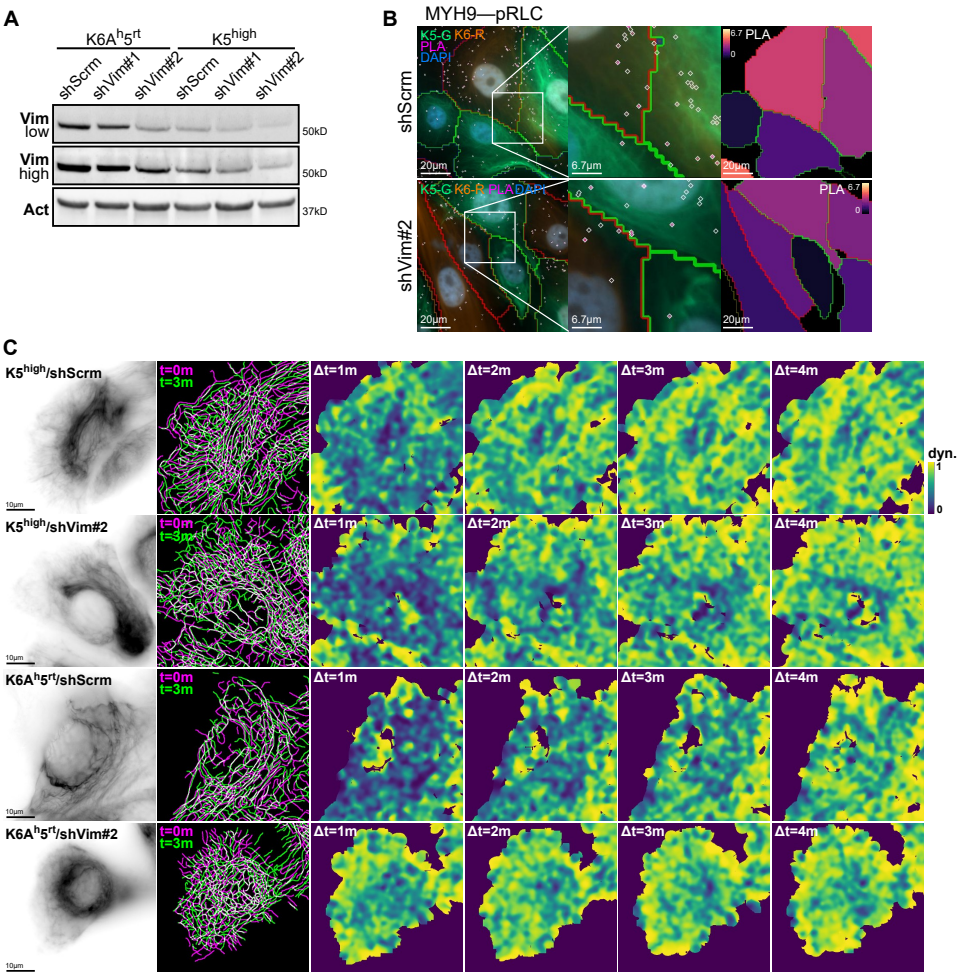

Figure S7. Non-filamentous vimentin mediates myosin activation and keratin filament dynamics.

A. Western blot analysis of vimentin knockdown by shRNA (shVim#1, shVim#2 versus scrambled control, shScrm) in keratinocytes expressing a chimeric keratin containing the head domain of K6A joined to the rod and tail of K5 (K6A^{h}5^{rt}) or full-length K5 (K5^{high}). The vimentin blot is displayed twice, with high and low brightness, to account for the different baseline vimentin levels in K5^{high} and K6A^{h}5^{rt} cells. See also Figure 7I for an alternate display of this blot.

B. Proximity ligation assay (PLA) detecting myosin activation by colocalization of phosphorylated myosin regulatory light chain (pRLC) and non-muscle myosin heavy chain (MYH9) in K5^{high} and K6A^{high} cells upon expression of shVim#2 versus shScrm. Annotated images of K5^{high} (green outline) and K6A^{high} (red outline) cells. White diamonds, PLA detections. Heatmap, PLA density (detections per 100 µm^{2}). K5-G, K5-mNeonGreen; K6A-R, K6A-mRuby2. See also comparison of PLA detection densities in Figure 7N.

C. Keratin network dynamics scores in K6A^{h}5^{rt} cells and K5^{high} cells expressing shRNA targeting vimentin (shVim#2) versus scrambled control (shScrm). Example keratin filament images, filament segmentations, and filament dynamics score maps. See also quantification in Figure 7O.

Video 1. Wound-associated K6A supports migration in three dimensional epidermal cultures.

Paired epidermal cultures of opposite cell lines initially separated by a 500-μm gap and imaged live over 24.6 hours at a sampling rate of 12 minutes per frame. Playback at 12 frames per second. Green and red lines indicate the farthest extent of migration for each culture. See also Figure 3H-K.

Video 2. Uniform-population monolayer migration assays do not detect differences between K5^{high} and K6A^{high} cells.

Uniform-population monolayers of K5^{high} or K6A^{high} cells were scratched to create a wound and imaged live over 12.5 hours at a sampling rate of 6 minutes per frame. Playback at 30 frames per second. The migration front was segmented using a computer vision pipeline and local migration speeds computed in blocks of 15-μm side-length by particle image velocimetry (see Methods). See also Figure S2A-D.

Video 3. Mosaic monolayer migration assays reveal subtle differences between K5^{high} and K6A^{high} cells during migration.

A mixed population monolayer containing K5^{high}, K6A^{high}, K5^{high}/K6A^{high}, and K5^{low}/K6A^{low} cells were scratched to create a wound and imaged over 12.5 hours at a sampling rate of 6 minutes per frame. Playback at 30 frames per second. See also Figure 4A-F. Keratin expression regions in the monolayer were segmented based on the fluorescence signal from the tagged keratin constructs (left). Local migration speeds computed in blocks of 15-μm side-length by particle image velocimetry (right; see Methods).

Video 4. Wound-associated K6A supports a transient migration advantage in monolayers.

Pairwise comparison of average local migration speed between keratin expression regions relative to the global migration peak. Each point represents one scratch wound. Points located along the diagonal line indicate equal local migration speeds in the two keratin expression regions. Points above or below the diagonal indicate that one region is moving faster than the other. n = 36 scratch wounds. See also Figure 4E-F.

Video 5. Wound-associated K6A supports a transient migration advantage in single cells.

Individual keratinocytes were sparsely seeded and allowed to migrate without exogenous directional cues. Imaged over 18 hours at a sampling rate of 3 minutes per frame. Playback at 24 frames per second. See also Figure 4G-I.

Video 6. Wound-associated K6A alters keratin filament dynamics.

Keratin filaments in K5^{high}, K6A^{high} (plays first), and K5^{high}/K6A^{high} (plays second) cells were imaged live over 24 minutes at a sampling rate of 30 seconds per frame. Playback at 24 frames per second. Filament networks were segmented using a computer vision pipeline (see Methods). Filament segmentations are overlayed on the tagged keratin fluorescence images. See also Figures 5A-E and S3H-M.